

**CORRELATION OF STATIC AND PEAK DYNAMIC COULOMB FAILURE
STRESS CHANGE WITH MAINSHOCKS, AFTERSHOCKS, SEISMICITY
RATE CHANGE, AND TRIGGERED SLIP IN THE SALTON TROUGH**

Jeffrey D. Eddo and Kim B. Olsen

Dept. of Geological Sciences, San Diego State University

November 19, 2007

Abstract

Numerous studies have found good correlation of static Coulomb failure stress (ΔCFS) from large earthquakes with the occurrence of aftershocks and other earthquakes later in time. However, reasons for a less than perfect correlation includes the observation that aftershocks often occur in the ΔCFS shadow zones, and remote triggering of earthquakes is difficult to explain from relatively small ΔCFS values. Recently, complete or dynamic Coulomb failure stress, parameterized by its largest positive value (peak $\Delta CFS(t)$), has been proposed as an alternative triggering mechanism (Kilb, 2002). In order to quantify the ability of the ΔCFS and peak $\Delta CFS(t)$ distributions for large earthquakes to trigger other large earthquakes, aftershocks, and aseismic slip, we have modeled ΔCFS and peak $\Delta CFS(t)$ for four recent historical earthquakes in the Salton Trough area of the Imperial Valley, California (1968 M6.7 Borrego Mountain, 1979 M6.6 Imperial Valley, 1987 M6.6 Elmore Ranch, and M6.5 Superstition Hills), using a finite-difference method. A cross-correlation is calculated between the modeled stresses and seismicity rate change in terms of the Z -value (Habermann, 1983). Modeling results show that peak $\Delta CFS(t)$ provides significantly better correlation with later mainshocks, aftershocks, seismicity rate change, and triggered slip than ΔCFS for all four events. On average, peak $\Delta CFS(t)$ fits the seismicity rate change 26% better than ΔCFS for time periods up to a month after the mainshocks, and peak $\Delta CFS(t)$ correlates with aftershocks significantly better than ΔCFS up to two years after the mainshock events. Our results for the Salton Trough suggest that peak $\Delta CFS(t)$ may be a more robust and sensitive parameter for earthquake triggering estimation, as compared to ΔCFS calculations.

Introduction

Studies of earthquake triggering are important for gaining new insights into the physics of earthquake occurrence, which may eventually lead to advances in the field of earthquake prediction. Such studies often rely on various estimates of the Coulomb Failure Stress change during an earthquake, defined as

$$\Delta CFS(t) = \Delta \tau_{13}(t) + \mu(\Delta \tau_{33}(t) + \Delta P(t)), \quad (1)$$

where $\Delta\tau_{13}(t)$ is the shear stress on the failure plane, $\Delta\tau_{33}(t)$ is the normal stress, $P(t)$ is the pore fluid pressure, and μ is the coefficient of friction. The static CFS change ($\Delta CFS = \Delta CFS(t)$ for $t \rightarrow \infty$) has traditionally been used to explain triggering of aftershock distributions and other earthquake sequences, fault slip, and areas experiencing seismicity rate change (e.g. Stein, 1999; Kilb, 2003; King et al., 1994; Toda and Stein, 2001; Arnadottir, 2003; Du et al., 2003; Freed, 2005). ΔCFS estimates are permanent and primarily dependent on the final co-seismic slip distribution and fault geometry. Stein et al. (1992) found positive correlation between the static stress field, caused by several large historic earthquakes, and regions where aftershocks were concentrated. However, the static stress triggering hypothesis is controversial because the size of the static stress changes suggested to have triggered earthquakes are small (<1 bar) as compared to the atmospheric pressure at the Earth's surface (~ 1 bar). Moreover, aftershocks are frequently observed in the shadow zones of the static stress fields (e.g., King et al., 1994; Stein, 1999; Toda and Stein, 2001; Kilb et al., 2002). In another study, Du et al. (2003) observed that areas of increased ΔCFS correlated with areas where triggered slip occurred. However, they concluded that static stress changes were not the only mechanism responsible for the observed triggered slip. Thus, a better understanding of the role of stresses induced by large earthquakes on the triggering of other earthquakes is desired.

An alternative parameter that may provide clues toward such improved understanding is the complete or *dynamic* Coulomb failure stress change, $\Delta CFS(t)$ (see Equation 1), which is transient and often at least an order of magnitude larger than ΔCFS (Figure 1) (Kilb et al., 2002). Kilb et al., among others, posed a hypothesis that the dynamic stresses may advance aftershocks to failure by changing the aftershock faults' physical and/or chemical properties and/or its environs. $\Delta CFS(t)$, parameterized by its largest positive value (peak $\Delta CFS(t)$), has been proposed as an alternative triggering mechanism (Voisin et al., 2000; Gomberg et al., 2001; Kilb, 2002). Peak $\Delta CFS(t)$ estimates, in addition to the final slip dependence, have been shown to be strongly dependent on co-seismic source effects, such as rupture directivity (Kilb, 2002). This sensitivity to transient rupture effects suggests that peak $\Delta CFS(t)$, as compared to ΔCFS , may provide a better tool for predicting triggered earthquakes and aftershocks in a short time window following the main event (Gomberg et al., 2003; Kilb et al., 2000).

In this study we have modeled ΔCFS and peak $\Delta\text{CFS}(t)$ distributions for four recent historical earthquakes (1968 M6.7 Borrego Mountain, 1979 M6.6 Imperial Valley, 1987 M6.6 Elmore Ranch, and M6.5 Superstition Hills). The study area is located in the Salton Trough of the Imperial Valley, California (Figure 2). For this area, ΔCFS and peak $\Delta\text{CFS}(t)$ distributions induced by the mainshock ruptures are resolved on orientations given by focal mechanisms of other large historical events for assessment of earthquake triggering. Additionally, ΔCFS and peak $\Delta\text{CFS}(t)$ distributions are resolved on optimally oriented failure planes (e.g., King et al., 1994) and compared with aftershock distributions spanning a day, a week, a month, a year, and two years after the mainshocks. A cross-correlation is calculated between the modeled stresses and the seismicity rate change for these time periods in terms of the Z-value (Habermann, 1983) with a background seismicity rate removed. Finally, we examine the correlation of modeled ΔCFS and peak $\Delta\text{CFS}(t)$ distributions with recorded triggered surface slip on the San Andreas fault (SAF), the Clark fault (CF), the Coyote Creek fault (CCF), the Elmore Ranch fault (ERF), the Superstition Hills fault (SHF), the Superstition Mountain fault (SMF), and the Imperial fault (IF). In the Appendix, we examine the sensitivity of our results to selected model parameters, such as the apparent coefficient of friction, poroelastic model, velocity model, and rupture velocity, in terms of the cross-correlation between the modeled stresses and seismicity rate change.

Methodology

Forward Modeling of Stresses

We have modeled ΔCFS and peak $\Delta\text{CFS}(t)$ using heterogeneous slip distributions derived from strong ground-motion and geodetic inversions for the 1968 M6.7 Borrego Mountain (Heaton and Helmberger, 1977) (Figure 3a), the 1979 M6.6 Imperial Valley (Hartzell and Heaton, 1983) (Figure 3b), and the 1987 M6.6 Elmore Ranch and M6.5 Superstition Hills (Wald et al., 1990; Larsen et al., 1992) (Figure 3c-d) earthquakes in a 150 by 150 km area of southern California (see Figure 2). We used a fourth-order staggered-grid finite-difference method with a grid spacing of 400 m throughout the model, including anelastic attenuation (Day et al., 1998; Day and Bradley, 2001) and the Southern California Earthquake Center (SCEC) 3-D Community Velocity Model (CVM) Version 4.0 (Figure 4). The lowest S-wave velocity included in the model was 1 km/s due to computational

limitations. The stresses for the Borrego Mountain (BM), Imperial Valley (IV), and Elmore Ranch (ER)-Superstition Hills (SH) sequence (ERSH) were calculated at depths of 6 km, 5km, and 6 km, respectively, which correspond to the depths containing most of the aftershock seismicity. All ΔCFS and peak $\Delta\text{CFS}(t)$ calculations used a friction coefficient of 0.4, unless otherwise specified. Since SH occurred 11.4 hours after ER, the stress distributions for ER and SH were computed separately but added together because of the difficulty in separating aftershocks and foreshocks between the two ruptures. For the correlation with aftershocks, ΔCFS and peak $\Delta\text{CFS}(t)$ distributions were resolved on optimally oriented failure planes by adding a 10 bar regional compressive stress, oriented N9°E, to the earthquake-induced stresses (King et al, 1994; Cocco et al., 2000; Holland, 2002). Stress distributions used to evaluate mainshock triggering were resolved on orientations given by focal mechanisms of the triggered mainshocks. The stresses used to correlate triggered surface slip were resolved on the ruptured mainshock faults themselves, which were similar in orientation to the surrounding faults experiencing triggered slip. In addition, forward modeling of both ΔCFS and peak $\Delta\text{CFS}(t)$ was conducted using the source parameters listed in Table 1. A Gaussian source-time function with a maximum frequency of 0.5 Hz was applied to each sub-fault with a constant rupture velocity. However, due to computational limitations, higher frequencies were not resolved.

Correlation of Seismicity Rate Change with Stresses

Seismicity rate change in terms of the Z-value (Habermann, 1983) was calculated using ZMAP software developed by Wiemer and Zuniga (1994). This measure was chosen to provide a general spatial overview of main seismicity rate (number of earthquakes occurring in a specified time interval) changes in the aftershock catalogs. The Z-value, by definition, is a measure of the statistical significance of the seismicity rate change, rather than the seismicity rate change value relative to expected random error (Toda and Stein, 2002). The Z-value or Z-statistic measure,

$$Z = \frac{R1 - R2}{\sqrt{\frac{S1}{N1} + \frac{S2}{N2}}}, \quad (2)$$

provides the significance of the difference between the mean seismicity rate change within a

time window ($R1$) and the background rate ($R2$), which is defined as the mean rate prior to the mainshock event. $S1$ and $S2$ are the variances of the means and $N1$ and $N2$ are the corresponding number of aftershocks and background events included, respectively (Chouliaras and Stavrakakis, 2001). Thus, the Z -value is a standard deviate and measures the spread of the data about the mean. If the seismicity rate change is close to the mean change, the Z -value is small, and vice versa. Note that negative Z -values indicate rate increases.

For this study, the Z -value maps are calculated for a day, a week, a month, a year, and two years after the mainshocks with a background rate in a period prior to the mainshock events subtracted. The background seismicity rate change was removed to minimize bias toward triggering. Additionally, background periods were selected that included no foreshocks or gaps in aftershock reporting or recording. Background periods which appeared to best represent the seismicity rate prior to the mainshocks were selected. We included only background and aftershock events in seismicity rate changes with magnitude equal to or larger than 2.1, the highest magnitude of completeness (M_c) for our dataset. This M_c was applied to help remove background seismicity and to minimize the effects of any secondary aftershocks (aftershocks triggered by other adjacent aftershocks).

The study area was divided into a grid with a spacing of 0.05° for both latitude and longitude. A circle was assigned around each grid point with a 5 km radius in order to include a reasonable number of earthquakes with magnitudes greater than or equal to M_c . This radius was chosen because it provided an optimal spatial coverage consistent with the extent of the aftershock distributions out of all the radii experimented for interpolation (from 0.005° to 0.5°). The Z -values were then calculated and interpolated to allow for correlation with the Coulomb Failure stress distributions. A cross-correlation measure was chosen because it takes into account the stress and seismicity rate change gradients, which minimizes bias due to the fact that peak $\Delta CFS(t)$ is positive over a larger portion of the region as compared to ΔCFS , thus making a baseline correlation to a random seismicity rate change insignificant and unnecessary. The correlation coefficient between a failure stress parameter S (peak $\Delta CFS(t)$ or ΔCFS) and the Z -value was calculated as

$$R = \frac{\sum_{i=1}^n (Z_i - \bar{Z}) \cdot (S_i - \bar{S})}{\sqrt{\sum_{i=1}^n (Z_i - \bar{Z}) \cdot \sum_{i=1}^n (S_i - \bar{S})}}, \quad (3)$$

where n is the number of grid points and \bar{Z} and \bar{S} denote the mean values of Z and S , respectively. The coefficient of determination or goodness of fit measure, R^2 (Cameron and Windmeijer, 1997), was calculated in percentage to express the significance of the correlation.

If both positive and negative ΔCFS values were included in the correlation calculated from Equation (1), we obtained negative correlation with seismicity rate changes for all time periods because of the anti-correlation with the stress shadow (or area of negative ΔCFS). This anti-correlation was due to the absence of seismicity rate decreases, which made it difficult to provide a fair comparison between ΔCFS and peak $\Delta\text{CFS}(t)$ with respect to triggering seismicity rate change. Thus, we decided to include only positive ΔCFS values in the correlation with Z -values. This also helped counterbalance the fact that the correlation of seismicity rate change with peak $\Delta\text{CFS}(t)$ can be less stringent than that of ΔCFS because of the large areal extent of the peak $\Delta\text{CFS}(t)$ distributions.

Triggering of Mainshocks

Numerous studies investigating stress triggering have shown epicenters of triggered mainshocks to correlate with areas of positive ΔCFS (e.g. King et al., 1994; Freed, 2005). ΔCFS often correlates with triggered seismicity at relatively close proximity to the triggering mainshock fault, but much weaker correlation is found with triggered events at larger distances (remote triggering). Peak $\Delta\text{CFS}(t)$, on the other hand, which is induced by the passage of seismic waves, has proven to be a more robust parameter for remote triggering, especially since it includes the effects of rupture directivity (Kilb, 2002). In this section we compare the ability of ΔCFS and peak $\Delta\text{CFS}(t)$ to predict mainshock locations. Particularly, we evaluate the potential of the 1968 BM to influence triggering of the 1979 IV in addition to the potential of the IV triggering the 1981 Westmorland, 1987 ER, and SH events. Additionally, the potential of both ΔCFS and peak $\Delta\text{CFS}(t)$ from ER to trigger SH approximately 11.4 hours later is evaluated. All ΔCFS and peak $\Delta\text{CFS}(t)$ distributions compared with triggered mainshock epicenters are resolved on the orientation of the

triggered mainshock faults rather than on the triggering mainshock fault plane or optimally oriented failure planes. This is done to ensure that the stresses are consistent with the triggered mainshock focal mechanisms. Since there are no constraints on the length of time that ΔCFS and peak $\Delta\text{CFS}(t)$ may effect earthquake triggering and no rate and state conditions are applied, we assume no time constraints for mainshock triggering after prior mainshocks.

ΔCFS and peak $\Delta\text{CFS}(t)$ distributions induced by BM were modeled to evaluate triggering of IV, which occurred approximately 11 years after the BM rupture. ΔCFS and peak $\Delta\text{CFS}(t)$ calculated for this event were resolved on the dextral IF fault plane striking N37°W. The modeling results show that the epicenter of IV is too far from any significant positive ΔCFS induced by BM (Figure 5a). However, it is possible that peak $\Delta\text{CFS}(t)$ has advanced triggering of the IV event (Figure 5b).

The 1981 M5.9 Westmorland earthquake occurred in the Brawley Seismic Zone just northwest of the Imperial fault. This event occurred in line with rupture directivity induced by the 1979 IV event in the middle of the aftershock distribution triggered by IV (Sharp et al., 1986). ΔCFS and peak $\Delta\text{CFS}(t)$ induced by the IV event were calculated and resolved on the left-lateral strike-slip fault plane of the 1981 Westmorland earthquake oriented N64°E, which is conjugate to the IF. The modeled ΔCFS distribution shows no correlation with the Westmorland epicenter (Figure 6a) while the peak $\Delta\text{CFS}(t)$ shows a positive correlation with the Westmorland epicenter, which is attributed to rupture directivity (Figure 6b).

The 1987 M6.6 ER and M6.5 SH events were also evaluated for possible triggering advancement by the 1979 M6.6 IV earthquake. The first event of the sequence was the left-lateral ER and the second was the right-lateral SH, which occurred approximately 11.4 hours after ER. SH was likely triggered more directly by ΔCFS and/or peak $\Delta\text{CFS}(t)$ from ER because of the close temporal and spatial proximity between the two earthquakes (Figure 7). The ERS sequence may also have been influenced by the 1981 M5.9 Westmorland event as parts of the IF and SHF displayed dextral surface displacement shortly after the occurrence of this event (Sharp et al, 1986). However, lack of surface rupture as well as rupture extent made modeling of stresses induced by the Westmorland event unfeasible.

ΔCFS and peak $\Delta\text{CFS}(t)$ were calculated for the IV event and resolved on the N40°E striking left-lateral ER fault plane and the N53°W right-lateral SH fault plane to be consistent

with focal mechanisms. The modeled ΔCFS distributions provided no positive correlation with the ER and SH epicenters (Figure 8). However, the peak $\Delta\text{CFS}(t)$ shows positive correlation with ER and SH epicenters, despite the fact that the stresses were resolved on conjugate planes. Thus, these positive correlations appear to be attributable to rupture directivity.

Triggering of Aftershocks and Seismicity Rate Change

Only a few studies have correlated both ΔCFS and peak $\Delta\text{CFS}(t)$ with aftershock distributions (Kilb, 2003; Kilb et al., 2002; Kilb, 2000). In addition, few studies have evaluated the change in correlation between stress distributions and aftershock seismicity or seismicity rate change over time after large earthquakes (e.g., Toda and Stein, 2001; Ma et al., 2005). In this section we evaluate the performance of both ΔCFS and peak $\Delta\text{CFS}(t)$ in triggering aftershocks and seismicity rate change over several different time periods after BM, IV, ER and SH. Tables 2a and 2b provide the goodness of fit between the modeled stress distributions for each earthquake and seismicity rate change for time periods of a day, a week, a month, a year, and two years after the events. Shorter time periods were neglected because spatial sampling was too sparse to compute reliable seismicity rate change estimates. Note that because of potential influence from the 1981 M5.9 Westmorland earthquake, which occurred approximately 1.5 years after IV, and gaps in aftershock reporting or recording occurring 2.5 months after IV, induced stresses from IV are only correlated with seismicity rate changes up to 2.5 months after the mainshock event.

Overall, ΔCFS only provides significant goodness of fit (>55%) with seismicity rate change for a day to a week after the mainshocks. On the other hand, peak $\Delta\text{CFS}(t)$ provides significant fit with seismicity rate change for a day to a month after the four mainshocks considered in this study. Both ΔCFS and peak $\Delta\text{CFS}(t)$ distributions along with aftershocks and the seismicity rate change for a month after the mainshocks are shown in Figures 9 through 11. Despite a low goodness of fit measures between BM and ERSH stress distributions and seismicity rate changes for a year and two years after the mainshocks, peak $\Delta\text{CFS}(t)$ distributions for both events still provide a reasonable qualitative fit to the aftershock distributions (Figures 12 and 13) for these periods of time.

Correlation of Stresses With Triggered Slip

Triggered (aseismic) slip by large earthquakes has been observed for many historical events in the Salton Trough, and correlated with ΔCFS . One of these studies, Du et al. (2003), concluded that ΔCFS either does not trigger slip or is not the only triggering mechanism. Here, we assess the correlation of both ΔCFS and peak $\Delta\text{CFS}(t)$ with triggered surface slip on surrounding faults for the 1986 BM, 1979 IV, and 1987 ER and SH events. All of these events have well documented observations of triggered surface slip available, thus providing an excellent opportunity to investigate the hypothesis posed by Du et al. 2003.

ΔCFS and peak $\Delta\text{CFS}(t)$ are calculated and resolved on the triggering earthquakes' fault planes, except for the left-lateral ER event. This is a reasonable assumption considering the faults that experienced triggered slip all generate right-lateral motion and are reasonably similar in strike (by $\pm 15^\circ$). Thus, the stress distributions for the ER event are simply resolved on faults with the same orientation as the SH event for consistency. ΔCFS and peak $\Delta\text{CFS}(t)$ distributions for BM, IV, and ERS_H are only qualitatively compared with mapped surface slip since the surface observations provide only a small glimpse of the total triggered slip. In particular, we assess the potential of BM ΔCFS and peak $\Delta\text{CFS}(t)$ in triggering slip on the SAF, SHF, and IF. We also compare IV stresses with triggered slip on the SAF and SHF, and ERS_H stresses with triggered slip on the SAF, CCF, and IF.

Triggered Slip Associated with BM

The M6.8 BM earthquake occurred on April 9, 1968 on the CCF and Borrego Mountain Fault (BMF) strands of the southern San Jacinto Fault Zone (SJFZ). Just four days after the earthquake, triggered slip was observed on the SAF, SH, and IF (Allen et al., 1972). This was the first documented example of triggered slip by seismic shaking far from a mainshock rupture (Allen et al., 1972). Allen et al. inferred that dynamic strain (or stress) is most likely the cause of the triggered slip since dynamic strain was estimated to be much larger than the static strain. Moreover, the orientation of static strain at the SAF was different than that for the observed displacement. Here, we attempt to test this hypothesis by an evaluation of whether slip was triggered by ΔCFS and/or peak $\Delta\text{CFS}(t)$.

Approximately 14 km of triggered slip occurred discontinuously along 30 km of the SAF shortly after the BM event. The average observed triggered displacement on the SAF ranged from 5 mm to 10 mm and the maximum displacement was 13 mm adjacent to the Painted Canyon at the northernmost displaced segment of the SAF (Allen et al., 1971; Sieh, 1982). Additionally, triggered slip was observed on the SHF with a maximum slip of ~ 25 mm across 23 km of the fault zone length. The largest displacements, which were >13 mm, occurred between 2-6 km from the southeast end and 3-5 km from the northwest end. The lowest values of displacement, 4-10 mm, occurred on the central portion of the fault zone (Allen et al., 1972). In addition, the IF showed approximately 20 mm of triggered slip along ~ 22 -30 km of its 60 km mapped length from the 1940 rupture. The minimum and maximum observed slip on the IF was 8 mm at the northwest end and 13 mm at the southeast end, respectively (Figure 14).

Figure 14a shows that BM Δ CFS appears to provide no correlation with mapped triggered slip. However, if a more realistic slip distribution that varied with depth were used, it is possible that positive Δ CFS may show some positive correlation with triggered slip on at least part of the SHF. The peak Δ CFS(t), on the other hand, provided reasonably positive correlation with triggered slip on all the faults (Figure 14b), with the exception of the northernmost portion of slip on the SAF where peak Δ CFS(t) is negligible. However, all of the triggered slip on the SAF may correlate better with BM peak Δ CFS(t) if a more accurate slip distribution is used. In summary, the positive correlation between BM peak Δ CFS(t) and triggered slip on surrounding faults supports the hypothesis by Allen et al. (1971), which infers that dynamic stress (or strain) was likely the triggering mechanism. This is also supported by the lack of positive correlation between BM Δ CFS and triggered slip.

Triggered Slip Associated with IV

The M6.6 IV earthquake occurred on October 15, 1979 with epicentral location in northern Mexico. This event was felt as far as Las Vegas and the Pacific Ocean (Johnson et al., 1982) and triggered slip occurred on nearly the same segments of the SAF and SHF as observed for the 1968 BM earthquake (Fruis, 1982; Sieh, 1982). Surface displacements were discovered four days after the BM event along the entire 23 km mapped length of the SHF

(Fruis, 1982). The observed dextral slip on the SHF was between 1-22 mm with maximum slip between 4-10 km of the northwest fault end (Fruis, 1982). Triggered slip was also observed on the SAF more than 90 km north of the IV mainshock (Sieh, 1982), with extent and amount of slip on the SAF generally mimicing that associated with the 1968 BM event. An average dextral slip of 4 mm was observed on the southern portion of the SAF, just east of the Salton Sea. In addition, maximum dextral slip of 10 mm was observed on the northernmost displaced segment of the SAF (Figure 15).

As observed with the 1968 BM event, triggered slip only appears to show positive correlation with the peak $\Delta\text{CFS}(t)$ (see Figure 15), which is strongly associated with the rupture directivity. Our results suggest that ΔCFS may have had little or no role in triggering slip associated with the IV event.

Triggered Slip Associated with ERSH

The M6.6 left-lateral strike-slip ER earthquake ruptured on November 24, 1987. This event was followed by the M6.5 SH earthquake, which ruptured at the northwest junction with ER (Magistrale et al., 1989), 11.4 hours later. This complex earthquake sequence triggered slip observed on several surrounding faults including the SAF, CCF, and IF. For example, McGill et al. (1989) observed a surface displacement of 6.4 mm on the Caltech alignment array located at the northernmost displaced segment of the SAF. Additionally, an average dextral slip of 3 mm was observed on the larger segment of SAF, just east of the Salton Sea on the Salt Creek array despite the fact that no surface breaks were observed. Hudnut and Clark (1989) observed a maximum 15 mm of triggered slip along a 3 km segment of the central break of the CCF. Triggered slip on the IF was also observed just east of the CCF. The northernmost segment of the IF revealed a maximum surface displacement of 31 mm (McGill et al., 1989). In addition, the central segment of the IF showed an average displacement of 15 mm with the southernmost terminus displaying a tapered slip averaging 6 mm (Figure 16).

As with the 1968 BM and 1979 IV earthquakes, Figure 16 shows the 1987 ERSH sequence provides significantly better peak $\Delta\text{CFS}(t)$ correlation with triggered slip than ΔCFS , although the very small positive ΔCFS may have contributed slightly to slip at the northwestern-most tip of the IF. Nonetheless, in contrast to ERSH ΔCFS , peak $\Delta\text{CFS}(t)$

provides reasonably positive correlation with triggered slip on all of the surrounding faults as all of the observed triggered slip lies in areas of substantially high peak $\Delta\text{CFS}(t)$

Discussion and Conclusions

Our objective of this study was to assess the seismic triggering potential of both ΔCFS and peak $\Delta\text{CFS}(t)$ for four large historical earthquakes in the Salton Trough, namely the 1968 M6.7 Borrego Mountain, 1979 M6.6 Imperial Valley, 1987 M6.6 Elmore Ranch, and M6.5 Superstition Hills earthquakes. Our modeling results show that peak $\Delta\text{CFS}(t)$ provides significantly better correlation with mainshocks, aftershocks, seismicity rate change, and triggered slip than ΔCFS for all four events. Both ΔCFS and peak $\Delta\text{CFS}(t)$ provided significant goodness of fit (>55%) with seismicity rate change up to a month after the mainshocks, with decreasing correlation for longer time periods. However, on average, the peak $\Delta\text{CFS}(t)$ fits the seismicity rate change 26% better than ΔCFS for time periods up to a month after the mainshocks, and peak $\Delta\text{CFS}(t)$ correlates with aftershocks significantly better than ΔCFS up to two years after the mainshock events. This implies that peak $\Delta\text{CFS}(t)$ may affect aftershock seismicity years after mainshock events where ΔCFS does not.

Since ΔCFS represent permanent stress changes it is reasonable to assume a triggering delay, even up to years after the mainshock. Peak $\Delta\text{CFS}(t)$, on the other hand, are transient changes, and it is expected that any resulting triggering is contemporary with the passing seismic waves, or relatively shortly after the mainshock. Thus, the improved performance of peak $\Delta\text{CFS}(t)$ over ΔCFS as a parameter for triggering mainshocks and aftershocks with a significant time delay was not expected, and our results imply that dynamic stresses may advance failure by altering a fault's physical/chemical properties or its environs irreversibly. Parsons (2005) proposed a possible mechanism for significantly delayed triggering by dynamic stresses was proposed by in which the frictional properties were altered in the surrounding faults. Particularly, Parsons modeling showed that a reduction of the slip weakening distance assuming a rate-and-state friction law could decrease the time to failure for the next event. Parsons also speculated that the most likely process for such frictional change was related to strain-induced compaction or fluid migration affecting the contact area and thus the slip weakening distance in the fault zone. Future studies should further test this hypothesis.

At least for the BM event, the peak $\Delta\text{CFS}(t)$ with (with $\mu' = 0.75$, see Appendix) * is capable of providing a goodness of fit with seismicity rate change $>55\%$ up to two years after the mainshock. However, more studies of this type are needed to make any further conclusions regarding the effectiveness of triggering spatially and temporally by peak $\Delta\text{CFS}(t)$ compared to ΔCFS . Nevertheless, our results provide a strong case for the validity of applying the peak $\Delta\text{CFS}(t)$ measure for earthquake triggering studies.

The overall favored performance of the peak $\Delta\text{CFS}(t)$ may be primarily attributed to its strong sensitivity to rupture parameters as well as to the 3D crustal velocity model. It should also be noted that the sensitivity to the coefficient of friction, poroelastic parameters, and crustal velocity model in terms of the goodness of fit with seismicity rate change, is stronger for peak $\Delta\text{CFS}(t)$ (up to 20%), as compared to ΔCFS (up to 11%) (see Appendix). Thus, peak $\Delta\text{CFS}(t)$ appears as a more flexible triggering parameter as compared to ΔCFS . Both ΔCFS and peak $\Delta\text{CFS}(t)$ appear to affect aftershock seismicity close to the mainshock ruptures, but peak $\Delta\text{CFS}(t)$ appears to be the primary parameter controlling remotely triggered aftershocks (defined by a minimum distance of 20 km from the mainshock) which can occur later in time. Additionally, peak $\Delta\text{CFS}(t)$ provides better correlation with seismicity rate change than ΔCFS for all of the earthquakes. This is particularly the case for IV, where static stresses induced by IV provide insignificant correlation with seismicity rate change and peak $\Delta\text{CFS}(t)$ shows strikingly significant correlation with seismicity rate change (see Tables 2a and 2b and Figure 10). This may imply the peak $\Delta\text{CFS}(t)$ affects seismicity rate change to a larger extent than ΔCFS for some events, but this hypothesis needs further testing by comparing ΔCFS and peak $\Delta\text{CFS}(t)$ for other earthquakes in different geographic locations.

Our study also indicates that the stress distributions induced by the BM, IV, and ERS sequences may have significantly advanced the southernmost parts of SAF and SJFZ toward failure. In particular, the ERS peak $\Delta\text{CFS}(t)$ appears to provide a large area of high stress increase of up to 2 bars in those areas. The southernmost 200-km stretch of the SAF has not produced a large earthquake since 1690 (Weldon et al., 2004), and recent computer simulations suggest that such an event, particularly with nucleation toward the southern end of the fault, could generate strong shaking in the greater Los Angeles area (Olsen et al., 2006).

One inherent limitation of our study is that we do not account for rate and state conditions (Gomberg et al., 1998) or viscoelastic relaxation (Vergnolle et al., 2003) potentially advancing nearby faults toward failure. Another concern about the comparisons in this study is the potential bias associated with the large area of positive peak $\Delta\text{CFS}(t)$. We addressed this issue by cross-correlating both static and dynamic stresses with random distributions representing seismicity rate change. We found that the correlations for both stress distributions were either negative or very insignificant ($<0.4\%$) indicating that peak $\Delta\text{CFS}(t)$ is not significantly biased for our cross-correlation calculations. Finally, refined estimates of the apparent coefficient of friction, poroelastic parameters, and rupture velocity may change the conclusions to some extent (see Appendix).

For improvement of this type of study, future studies should use more constrained rupture parameters (especially rupture velocity) if possible along with a 3-D crustal velocity model, at least for peak $\Delta\text{CFS}(t)$ calculations. It might also be useful to compute seismicity rate changes by other means rather than the Beta statistic or Z-value measures (used here) which have been most commonly applied in previous studies. These proposed improvements could provide a broader and more realistic approach to understanding the earthquake triggering process.

References

- Allen, C. R., M. Wyss, J. N. Brune, A. Grantz, and R. E. Wallace (1972). Displacements on the Imperial, Superstition Hills, and San Andreas faults triggered by the Borrego Mountain earthquake, *U.S. Geol. Surv. Profess. Paper 787*, 87-104.
- Antonioli, A., Belardinelli, M.E., and Cocco, M. (2004). Modelling dynamic stress changes caused by an extended rupture in an elastic stratified halfspace, *Geophys. J. Int.*, 157(1), 229-244.
- Archuleta, R.A. (1984). Faulting model for the 1979 Imperial Valley earthquake, *J. Geophys. Res.*, 89, 4559-4585.
- Árnadóttir, Th., S. Jónsson, R. Pedersen, and G.B. Gudmundsson (2003). Coulomb stress changes in the South Iceland Seismic Zone due to two large earthquakes in June 2000, AGU-EUG-EGS Joint assembly, Abstract G12-1TU4O-002, Nice, April 6-11, France.
- Beeler, N. M., R. W. Simpson, D. A. Lockner, and S. H. Hickman (2000). Pore fluid pressure, apparent friction and Coulomb failure, *J. Geophys. Res.*, 105, 25, 533-25, 554.

Bouchon, M., Toks, N., Karabulut, H., Bouin, M., Dietrich, M., Aktar, M. and Edie, M. (2000). Seismic imaging of the 1999 Izmit (Turkey) rupture inferred from the near-fault recordings. *Geophysical Research Letters* 27(18): doi: 10.1029/2000GL011761. issn: 0094-8276.

Bouchon, M. and Vallee, M. (2003). Observation of long supershear rupture during the magnitude 8.1 Kunlunshan earthquake. *Science*, 301(5634), 824-826.

Cameron, C.A. and F.G. Windmeijer (1997). An R-squared Measure of Goodness of Fit for some common Nonlinear Regression Models, *Journal of Econometrics*, 1997, 77, 2, 329-342.

Chouliaras, G., Stavrakakis, G.N. (2001). Current seismic quiescence in Greece: implications for seismic hazard. *J. Seismol.* 5, 595–608.

Cocco, M., C. Nostro, and G. Ekstrom (2000). Static stress changes and fault interaction during the 1997 Umbria-Marche earthquake sequence, *J. Seismol.*, 4, 501-516.

Day, S.M. (1998). Efficient simulation of constant Q using coarse-grained memory variables, *Bull. Seism. Soc. Am.* 88, 1051-1062.

Day, S.M., and C. Bradley (2001). Memory-efficient simulation of anelastic wave propagation, *Bull. Seism. Soc. Am.* 91, 520-531.

Du, W., L. R. Sykes, B. E. Shaw, and C. H. Scholz (2003). Triggered aseismic fault slip from nearby earthquakes, static or dynamic effect?, *J. Geophys. Res.*, 108, 2131, doi:10.1029/2002JB002008.

Dunham, E. M., and R. J. Archuleta (2004). Evidence for a supershear transient during the 2002 Denali fault earthquake, *Bull. Seism. Soc. Am.* 94, S256-S268.

Freed A.M. (2005). Earthquake triggering by static, dynamic, and postseismic stress transfer *Annu. Rev. Earth Planet. Sci.*, 33, p.335-367.

Fuis, G. S. (1982). Displacement on the Superstition Hills fault triggered by the earthquake, in The Imperial Valley Earthquake of October 15, 1979, *U.S. Geol. Surv. Profess. Paper 1254*, 145-154.

Gomberg, J., Beeler, N. M., Blanpied, M. L. & Bodin, P. (1998). Earthquake triggering by transient and static deformations. *J. Geophys. Res.* 103, 24, 411–426.

Gomberg, J., P.A. Reasenber, P. Bodin, and R.A. Harris (2001). Earthquake triggering by seismic waves following the Landers and Hector Mine earthquakes, *Nature*, 411, 462-466.

- Gomberg, J., Bodin, P. & Reasenber, P.A. (2003). Observing earthquakes triggered in the near field by dynamic deformations, *Bull. seism. Soc. Am.*, 93, 118–138.
- Habermann, R.E. (1983). Teleseismic detection in the Aleutian Island arc, *J. Geophys. Res.*, 88, 5056-5064.
- Hartzell, S. H. and T. H. Heaton (1983). Inversion of strong ground motion and teleseismic waveform data for the fault rupture history of the 1979 Imperial Valley, California, earthquake, *Bull. Seism. Soc. Am.* 73, 1553-1583.
- Heaton, T. It. and D. V. Helmberger (1977). A study of the strong ground motion of the Borrego Mountain, California, Earthquake, *Bull. Seism. Soc. Am.* 57,315-330.
- Holland, A. (2002). Microearthquake study of the Salton Sea geothermal field, California: Evidence of stress triggering, M.S. Thesis, Idaho National Engineering and Environmental laboratory.
- Hudnut, K. W., and M. M. Clark (1989). New slip along parts of the 1968 Coyote Creek fault rupture, California, *Bull. Seismol. Soc. Am.*, 79, 451–465.
- Johnson, C. E. and L. K. Hutton (1982). Aftershocks and pre-earthquake seismicity, in The Imperial Valley, California, Earthquake of October 15, 1979, *U.S. Geol. Surv. Prof. Paper 1254*, 59-76.
- Kilb, D. (2002). A strong correlation between induced peak dynamic Coulomb stress change from the 1992 M7.3 Landers, California, earthquake and the hypocenter of the 1999 M7.1 Hector Mine, California, earthquake, *J. Geophys. Res.*, 107, doi:10.1029/2001JB000678.
- Kilb, D., J. Gomberg, and P. Bodin (2000). Triggering of earthquake aftershocks by dynamic stresses, *Nature*, 408, 570-574.
- Kilb, D., J. Gomberg, and P. Bodin (2002). Aftershock triggering by complete Coulomb stress changes, *J. Geophys. Res.*, 107, 2001JB000202.
- Kilb, D. (2003). A strong correlation between induced peak dynamic Coulomb stress change from the 1992 M 7.3 Landers earthquake and the hypocenter of the 1999 M 7.1 Hector Mine earthquake, *J. Geophys. Res.* 108, B1 2012, doi 10.1029/2001JB000678.
- King G. C. P., R. S. Stein, and J. Lin (1994). Static stress changes and the triggering of earthquakes, *Bull. Seismol. Soc. Am.*, 84, 935-953.
- Larsen, S., R. Reilinger, H. Neugebauer, and W. Strange (1992). Global Positioning System Measurements of Deformations Associated with the 1987 Superstition Hills Earthquake - Evidence for Conjugate Faulting. *J. Geophys. Res.*, 97 (B4): 4885-4902.

Ma, K.F., Chan, C.H., and Stein, R. S. (2005). Response of seismicity to Coulomb stress triggers and shadows of the 1999 $M_w = 7.6$ Chi-Chi, Taiwan, earthquake, *J. Geophys. Res.*, Vol. 110, B05S19, doi:10.1029/2004JB003389.

Magistrale, H., L. Jones, and H. Kanamori (1989). The Superstition Hills, California, Earthquakes of 24 November 1987, *Bull. Seism. Soc. Am.* 79, 239-251.

McGill, S. F., C. R. Allen, K. W. Hudnut, D. C. Johnson, W. F. Miller, and K. E. Sieh (1989). Slip on the Superstition Hills fault and on nearby faults associated with the 24 November 1987 Elmore Desert Ranch and Superstition Hills earthquakes, southern California, *Bull. Seism. Soc. Am.* 79, 362-375.

Olsen, K.B. (1994). Simulation of three-dimensional wave propagation in the Salt Lake Basin, Ph.D. Thesis, University of Utah.

Olsen, K. B., S. M. Day, J. B. Minster, Y. Cui, A. Chourasia, M. Faerman, R. Moore, P. Maechling, and T. Jordan (2006). Strong shaking in Los Angeles expected from southern San Andreas earthquake, *Geophysical Research Letters*, 33, L07305, doi:10.1029/2005GL025472.

Parsons, T., R.S. Stein, R.W. Simpson, and P.A. Reasenber (1999). Stress sensitivity of fault seismicity: A comparison between limited-offset oblique and major strike-slip faults, *J. Geophys. Res.*, 104, 20,183-20, 202.

Perfettini, H., R. S. Stein, R. W. Simpson, and M. Cocco (1999), Stress transfer by the 1988–1989 $M = 5.3$ and 5.4 Lake Elsmar foreshocks to the Loma Prieta fault; unclamping at the site of peak main shock slip, *J. Geophys. Res.*, 104, 20, 169-20, 182.

Sharp, R. V., M. J. Rymer, and J. J. Lienkaemper (1986). Surface displacements on the Imperial and Superstition Hills faults triggered by the Westmorland, California, earthquake of 26 April 1981, *Bull. Seismol. Soc. Am.*, 76, 1838-1843.

Sieh, K. E. (1982). Slip along the San Andreas associated with the earthquake, in *The Imperial Valley Earthquake of October 15, 1979*, *U.S. Geol. Surv. Profess. Paper 1254*, 155-160.

Stein, R. S., G. C. P. King, and J. Lin (1992). Change in failure stress on the southern San Andreas fault system caused by the 1992 Magnitude=7.4 Landers earthquake, *Science*, 258, 1328-1332.

Stein, R.S. (1999). The role of stress transfer in earthquake occurrence, *Nature*, 402, 605-609.

Toda, S. and Stein, R.S. (2002). Response of the San Andreas Fault to the 1983 Coalinga-Nuñez Earthquakes: An Application of Interaction-based Probabilities for Parkfield, *J. Geophys. Res.* 107, 10.1029/2001JB000172.

Vergnolle, M., Pollitz, F. and Calais, E. (2003). Constraints on the viscosity of the continental crust and mantle from GPS measurements and postseismic deformation models in western Mongolia. *J. of Geophys. Res.* 108(B10): doi: 10.1029/2002JB002374. issn: 0148-0227.

Voisin, C., I. R. Ionescu, F. Cotton, and O. Scotti (2000). Dynamic versus static stress triggering and friction parameters: Inferences from the November 23, 1980, Irpinia earthquake, *J. Geophys. Res.*, 105, 21, 647-21, 659.

Wald, D.J., D.V. Helmberger, and S.H. Hartzell (1990). Rupture process of the 1987 Superstition Hills earthquake from the inversion of strong motion data, *Bull. Seismol. Soc. Amer.*, 80, 1079-1098.

Weldon, R., K. Scharer, T. Fumal, and G. Biasi (2004). Wrightwood and the earthquake cycle: What a long recurrence record tells us about how faults work, *Geol. Seism. Am.* 14, 4-10.

Wiemer, S. and F.R. Zuniga (1994). ZMAP-a software package to analyze seismicity. EOS, Transactions, Fall Meeting, AGU, 75, 456.

Tables

Table 1. Source Parameters (Heaton and Helmberger, 1977; Hartzell and Heaton, 1983; Larsen et al., 1992; Wald et al., 1990) for the BM, IV, ER, and SH Earthquakes

Event	Borrego Mountain (BM)	Imperial Valley (IV)	Elmore Ranch (ER)	Superstition Hills (SH)
Date	4/9/1968	10/15/1979	11/24/1987	11/24/1987
Epicenter Latitude	33.190	32.644	33.020	33.015
Epicenter Longitude	-116.129	-115.309	-115.690	-115.852
Focal Depth (km)	11	10	9	9
Magnitude	6.7	6.6	6.6	6.5
M_0 (Nm)	1.21E+19	8.64E+18	7.52E+18	6.57E+18
Rupture Length (km)	36	42	25	20
Strike ($^{\circ}$)	132	323	40	127
Dip ($^{\circ}$)	90	90	90	90
Rake ($^{\circ}$)	180	180	0	180
Rupture Velocity (km/s)	2.7	2.5	3	2.4

Table 2a. Percent Goodness of Fit Between Seismicity Rate Change and Static Coulomb Failure Stress Change For Various Time Periods After the Mainshocks

Time Period	BM	IV	ER+SH	Average
2 year	30	-	21	26
1 year	35	-	29	32

2.5 month	-	30	-	-
1 month	47	31	44	41
1 week	52	30	67	50
1 day	53	18	74	48

Table 2a. Percent Goodness of Fit Between Seismicity Rate Change and Peak Dynamic Coulomb Failure Stress Change For Various Time Periods After the Mainshocks

Time Period	BM	IV	ER+SH	Average
2 year	51	-	25	38
1 year	50	-	33	42
2.5 month	-	83	-	-
1 month	60	79	54	64
1 week	68	90	80	79
1 day	63	72	88	74

Appendix: **Model Parameter Sensitivity**

Sensitivity to the Apparent Coefficient of Friction

The apparent coefficient of friction (μ') used to obtain ΔCFS and peak $\Delta\text{CFS}(t)$ distributions up to this point was 0.4. The value of μ' is mostly unconstrained, and it has commonly been assumed that ΔCFS is only modestly sensitive to this parameter. However, some studies have shown that shear stress changes correlate better with triggered seismicity in some cases and normal stress changes correlate better in others (e.g. Perfettini et al., 1999; Parsons et al., 1999). In this section we quantify the effects of different values of μ' on the resulting ΔCFS and peak $\Delta\text{CFS}(t)$ distributions for the four earthquakes used in our study.

For the 1968 BM, 1979 IV, and 1987 ER and SH events, optimally oriented ΔCFS and peak $\Delta\text{CFS}(t)$ distributions with apparent coefficient of friction values of 0.75 and 0.4 were compared. ΔCFS with $\mu' = 0.75$ provided an overall increase in the goodness of fit with seismicity rate change up to 11% (Figure A1). Specifically, the ΔCFS goodness of fit with seismicity rate change for a month after the BM mainshock increased from 47% to 57%. Peak $\Delta\text{CFS}(t)$ showed even larger sensitivity to μ' . For example, peak $\Delta\text{CFS}(t)$ distributions with $\mu' = 0.75$ showed an increase in the goodness of fit with seismicity rate change up to 20% (Figure A1). In addition, the BM induced peak $\Delta\text{CFS}(t)$ distribution with $\mu' = 0.75$ provided reasonable improvement for all the associated time periods evaluated, including a year (from 50% to 60%) and two years (from 51% to 57%) after the BM mainshock. Thus, the refined goodness of fit measures suggest that peak $\Delta\text{CFS}(t)$ exhibits some potential to correlate with seismicity rate change years after some mainshock events where ΔCFS does not. Thus, peak $\Delta\text{CFS}(t)$ may be a more accurate parameter for earthquake triggering if the apparent coefficient of friction can be constrained.

Sensitivity to Poroelastic Parameters

In the previous sections we have assumed $\Delta P(t) = 0$, which requires the assumption of a constant apparent coefficient of friction that is applied in most CFS studies. This

assumption is intended to incorporate both friction and pore pressure effects into the earthquake rupture. However, μ' is only a material constant if the induced changes in pore pressure are proportional to the normal stress change across the failure plane (Beeler et al., 2000). This may not always be a safe assumption as pore pressure conditions can vary among different earthquakes. Thus, the aim of this section is to assess the effect of the isotropic poroelastic model

$$\Delta P(t) = -S \frac{1}{3} (\Delta \tau_{11}(t) + \Delta \tau_{22}(t) + \Delta \tau_{33}(t)), \quad (4)$$

where the pore pressure is proportional to the mean normal stress change and S is the Skempton coefficient, here and most commonly assumed to be 0.6.

Figure A2 shows the correlation of BM Δ CFS and peak Δ CFS(t) for $\Delta P(t) = 0$ with Z -value maps for a month after the mainshock. The Δ CFS distributions using the isotropic poroelastic model for all of the ruptures and aftershock time periods evaluated show a modest overall decrease in the goodness of fit with seismicity rate change (up to 7% as compared to a purely elastic model). The peak Δ CFS(t) distribution using the poroelastic model provided an overall decrease in fit up to 20% (see Figure A2). Thus, the peak Δ CFS(t) is more sensitive to poroelastic effects than Δ CFS. Nevertheless, these results imply that the constant apparent friction assumption is reasonably fit for the modeled mainshocks in this study. However, it is possible that poroelastic models may generate failure stresses that produce higher correlation with aftershocks for other earthquakes.

Sensitivity to Velocity Model

We have used a 3-D crustal velocity model of the Salton Trough area from the SCEC CVM V4.0 in our modeling of triggering potential of the Δ CFS and peak Δ CFS(t) fields. To our knowledge, this is the first time that a 3-D state-of-the-art velocity structure has been used to examine the triggering potential of peak Δ CFS(t), as previous studies have used homogeneous (Voisin et al., 2000) or at best, layered models (Kilb et al., 2002) of the underlying crustal material (Antonioli et al., 2004). In this section we compare our results for the 3-D model to those for a 1-D velocity model that varies only with depth, to explore the effect of the accuracy of the velocity model.

Figure A3 shows the correlation of BM Δ CFS for 1-D and 3-D models and the correlation of IV peak Δ CFS(t) for 1-D and 3-D models. Both Δ CFS and peak Δ CFS(t) distributions estimated from the 1-D velocity model show a decrease in the correlation with Z-value maps for all of the ruptures and all of the time periods evaluated after the mainshocks. For some events and time periods the goodness of fit with seismicity rate change is reduced by as much as 8% and 19% for Δ CFS and peak Δ CFS(t), respectively (see Figure A3). This implies that application of a 3-D velocity model can be essential to provide reasonable stress change estimates, particularly for peak Δ CFS(t) calculations where the amplification in the low-velocity sediments are found to affect the stress distribution (see the larger peak Δ CFS(t) for IV (Figure A3) in the Imperial Valley (Figure 4).

Rupture Velocity Sensitivity

The calculations of failure stresses for the four earthquakes in the Salton Trough in this study used rupture models constrained by seismological and geological observations. In particular, a constant sub-shear rupture velocity was estimated for IV, ER and SH from strong-motion inversion. These results are in agreement with the observation that on average, most large earthquakes tend to produce sub-shear rupture velocities. However, several seismological studies have suggested the occurrence of super-shear rupture propagation in strike-slip events (Archuleta, 1984; Bouchon et al., 2000; Bouchon and Vallee, 2003; Dunham and Archuleta, 2004). The constant sub-shear rupture velocity inferred for the IV, ER, and SH are likely strongly simplified results based on lack of resolution from the strong motion data, and the occurrence of local bursts of super-shear rupture propagation for the earthquakes is entirely possible. In fact, Archuleta (1984) found evidence of possible super-shear rupture propagation for IV. For this reason, we here explore the general effects of sub-shear and super-shear rupture velocities on the computed stresses. Since Δ CFS is mostly unaffected by co-seismic rupture effects, we concentrate our analysis on peak Δ CFS(t). To our knowledge, no previous studies have reported the effects of rupture velocity on peak Δ CFS(t).

Our tests for the rupture velocity use a right-lateral fault with a rupture length of 20 km with a dip of 90° with uniform slip of 1 m, linearly tapered to zero starting 5 km from the

edge. The modeled peak $\Delta\text{CFS}(t)$ distributions are resolved on the plane of the ruptured mainshock fault for a bilateral and unilateral rupture with constant apparent friction of 0.4. The stresses are computed in a homogenous velocity model without anelastic attenuation in order to isolate the effects of the rupture velocity. Figure A4 shows peak $\Delta\text{CFS}(t)$ including a sub-shear rupture velocity (2 km/s) and super-shear rupture velocity (4 km/s), which is 57% and 114% of the S-wave velocity structure, respectively. This shows that super-shear rupture velocities produce substantially higher peak $\Delta\text{CFS}(t)$ values than sub-shear rupture velocities. Moreover, a substantially larger area of high peak $\Delta\text{CFS}(t)$ is produced, in comparison with that from a sub-shear rupture, particularly for a unilateral rupture (see Figure A4). These results suggest that peak $\Delta\text{CFS}(t)$ is highly sensitive to rupture velocity and that a better constrained rupture velocity may significantly improve the correlation between peak $\Delta\text{CFS}(t)$ and seismicity rate change.

Figure Captions

Figure 1. The progression of the complete Coulomb stress change, $\Delta\text{CFS}(t)$, over time and distance. The double arrows show the peak $\Delta\text{CFS}(t)$, or dynamic stress values, and the ΔCFS or static stress values, which can be positive or negative (from Kilb et al., 2000).

Figure 2. Location map showing the study area of interest.

Figure 3. Slip distributions and source locations for BM (Heaton and Helmberger, 1977) (a), IV (Hartzell and Heaton, 1983) (b), ER (Larsen et al., 1992) (c), and SH (Wald et al., 1990) (d). The stars depict the hypocenters.

Figure 4. S-wave velocity structure at 1 km depth extracted from the 3-D velocity model (SCEC CVM V4.0) with epicenter locations of the modeled mainshocks (stars), associated rupture lengths (white lines), surface traces of other main faults (dotted lines), and the Salton Sea (magenta).

Figure 5. BM ΔCFS (a) and peak $\Delta\text{CFS}(t)$ (b) calculated at 6 km depth with the epicenter of the 1979 M6.6 IV earthquake shown to the southeast. The filled and open stars depict the BM and IV epicenters, respectively.

Figure 6. IV ΔCFS (a) and peak $\Delta\text{CFS}(t)$ (b) calculated at 5 km depth with the epicenter of the 1981 M5.9 Westmorland earthquake shown to the northwest. The filled and open stars depict the IV and Westmorland epicenters, respectively.

Figure 7. ER ΔCFS (a) and peak $\Delta\text{CFS}(t)$ (b) calculated at 6 km depth with the epicenter of the SH earthquake shown just southwest of ER. The filled and open stars depict the ER and SH epicenters, respectively.

Figure 8. IV ΔCFS (a) and peak $\Delta\text{CFS}(t)$ (b) calculated at 5 km depth with the epicenter of the 1987 M6.6 ER earthquake shown just south of the Salton Sea. (c) and (d) show ΔCFS and peak $\Delta\text{CFS}(t)$, respectively, with the location of the 1987 M6.5 SH earthquake, which occurred just 11.4 hours after ER. The filled star depicts the IV epicenter and the open stars depict the ER and SH epicenters.

Figure 9. BM Δ CFS with aftershocks spanning up to a month after the mainshock (a) and Δ CFS -0.8 bar (dashed) and 0.8 bar (solid) contours overlying the Z-value map calculated for the month after BM (b). The peak Δ CFS(t) with aftershocks spanning up to a month after the mainshock is shown in (c) and peak Δ CFS(t) one- (solid), two- (dashed), and three- (solid) bar contours overlying the Z-value map for a month after BM are shown in (d). The stars depict the BM epicenter.

Figure 10. IV Δ CFS with aftershocks spanning up to a month after the mainshock (a) and Δ CFS -0.8 bar (dashed) and 0.8 bar (solid) contours overlying the Z-value map calculated for the month after IV (b). The peak Δ CFS(t) with aftershocks spanning up to a month after the mainshock is shown in (c) and peak Δ CFS(t) one- (solid), two- (dashed), and three- (solid) bar contours overlying the Z-value map for a month after IV are shown in (d). The stars depict the IV epicenter.

Figure 11. ERSH Δ CFS with aftershocks spanning up to a month after the mainshocks (a) and Δ CFS -0.8 bar (dashed) and 0.8 bar (solid) contours overlying the Z-value map calculated for the month after ERSH (b). The peak Δ CFS(t) with aftershocks spanning up to a month after the mainshocks is shown in (c) and peak Δ CFS(t) one- (solid), two- (dashed), and three- (solid) bar contours overlying the Z-value map for a month after ERSH are shown in (d). The stars depict the ER and SH epicenters.

Figure 12. BM Δ CFS with aftershocks spanning up to a year after the mainshock (a) and Δ CFS -0.8 bar (dashed) and 0.8 bar (solid) contours overlying the Z-value map calculated for the year after BM (b). The peak Δ CFS(t) with aftershocks spanning up to a year after the mainshock is shown in (c) and peak Δ CFS(t) one- (solid), two- (dashed), and three (solid) bar contours overlying the Z-value map for a year after BM are shown in (d). The stars depict the BM epicenter.

Figure 13. ERSH Δ CFS with aftershocks spanning up to a year after the mainshocks (a) and Δ CFS -0.8 bar (dashed) and 0.8 bar (solid) contours overlying the Z-value map calculated for the year after ERSH (b). The peak Δ CFS(t) with aftershocks spanning up to a year after the mainshocks is shown in (c) and peak Δ CFS(t) one- (solid), two- (dashed), and three- (solid) bar contours overlying the Z-value map for a year after ERSH are shown in (d). The stars depict the ER and SH epicenters.

Figure 14. BM Δ CFS (a) and peak Δ CFS(t) (b) calculated at 6 km depth with mapped segments of observed triggered slip and approximate locations of minimum, maximum, and average slip values. The stars depict the BM epicenter.

Figure. 15 IV Δ CFS (a) and peak Δ CFS(t) (b) calculated at 5 km depth with mapped segments of observed triggered slip and approximate locations of minimum, maximum, and average slip values. The stars depict the IV epicenter.

Figure 16. ERSH Δ CFS (a) and peak Δ CFS(t) (b) calculated at 5 km depth with mapped segments of observed triggered slip and approximate locations of minimum, maximum, and average slip values. The stars depict the ER and SH epicenters.

Figure A1. Correlation of BM Δ CFS contours for 0.4 (a) and 0.75 (b) apparent coefficient of friction with Z-value maps for a month after BM. Correlation of BM peak Δ CFS(t) contours for 0.4 and 0.75 apparent coefficient of friction with Z-value maps for a month after BM is shown in (c) and (d), respectively. Goodness of fit measures are provided in the top right corners. The stars depict the BM epicenter.

Figure A2. Correlation of BM Δ CFS contours for $\Delta P(t) = 0$ (a) and a Skempton coefficient of 0.6 (b) with Z-value maps for a month after BM. Correlation of BM peak Δ CFS(t) contours for $\Delta P(t) = 0$ and a Skempton coefficient of 0.6 with Z-value maps for a month after BM are shown in (c) and (d), respectively. Goodness of fit measures are provided in the top right corners. The stars depict the BM epicenter.

Figure A3. Correlation for BM Δ CFS contours for a 3-D velocity model (a) and 1-D velocity model (b) with Z-value maps for a day after BM. Correlation of IV peak Δ CFS(t) contours for a 3-D velocity model and 1-D velocity model with Z-value maps for a week after IV is shown in (c) and (d), respectively. Goodness of fit measures are provided in the top right corners. The stars depict the epicenters.

Figure A4. Peak Δ CFS(t) distributions at 8 km depth for bilateral and unilateral ruptures applying sub-shear ((a) and (b)) and super-shear ((c) and (d)) rupture velocities, which are 57% and 114% of the homogenous S-wave velocity structure, respectively. The star depicts the epicenter.

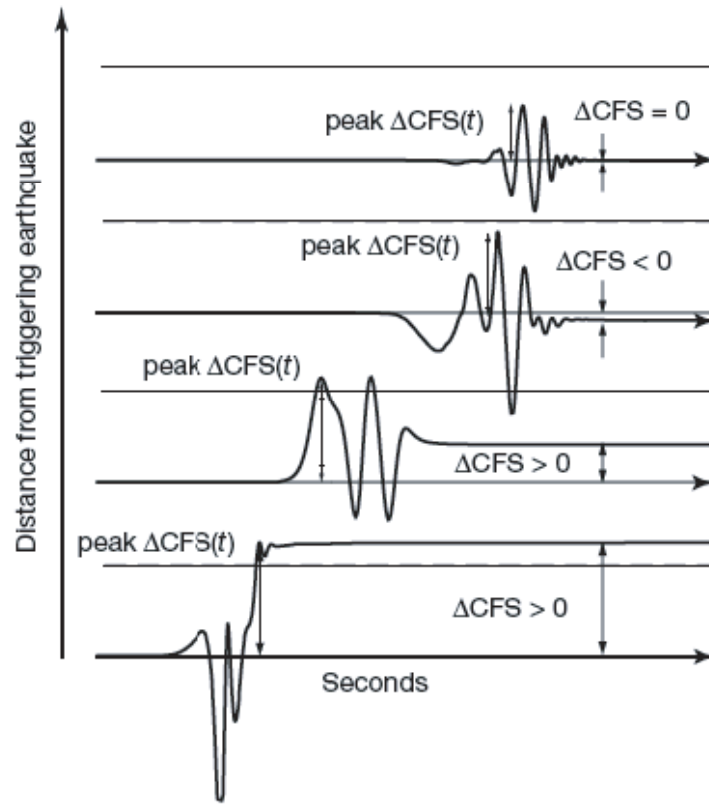


Figure 1



Figure 2

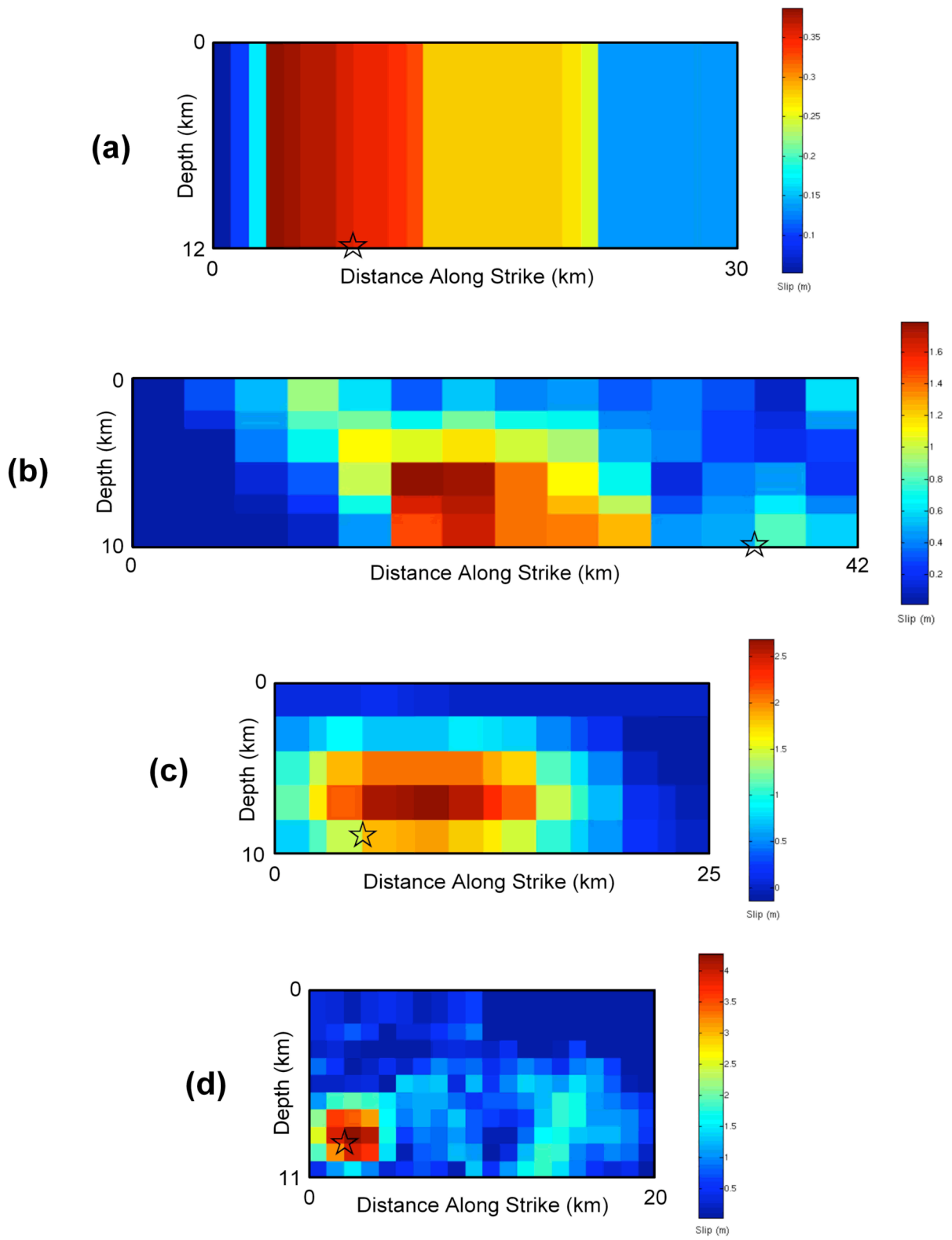


Figure 3

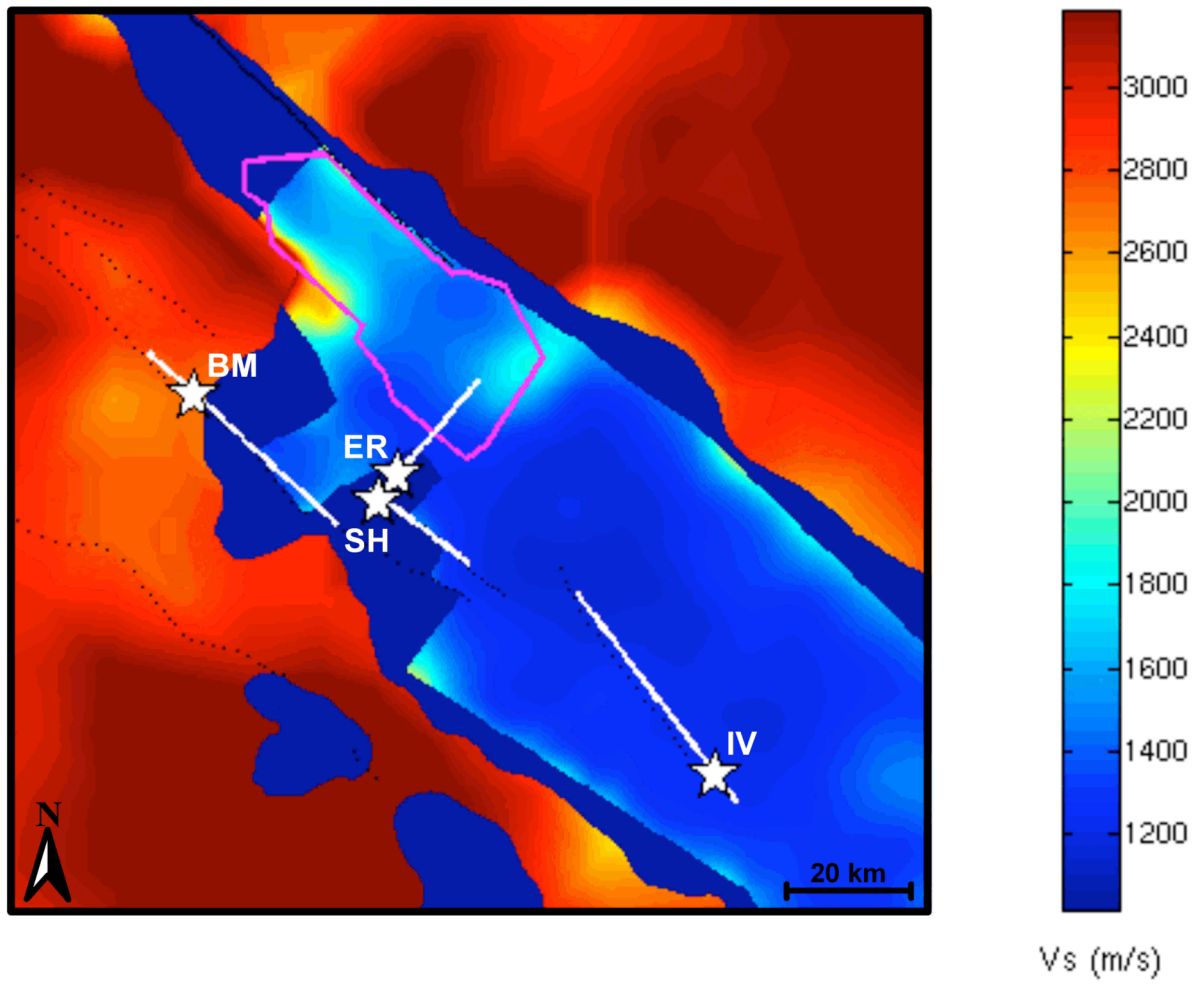


Figure 4

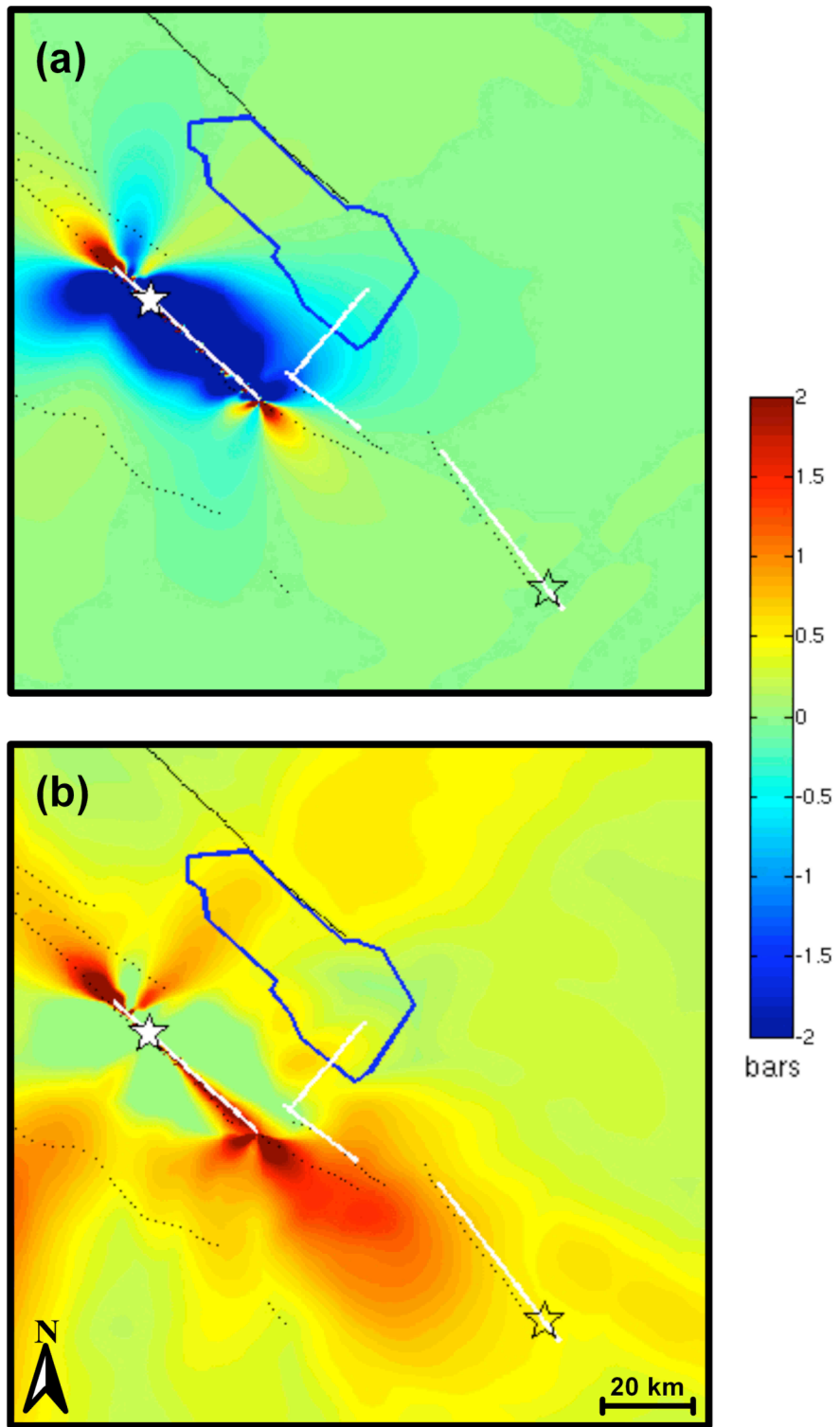


Figure 5

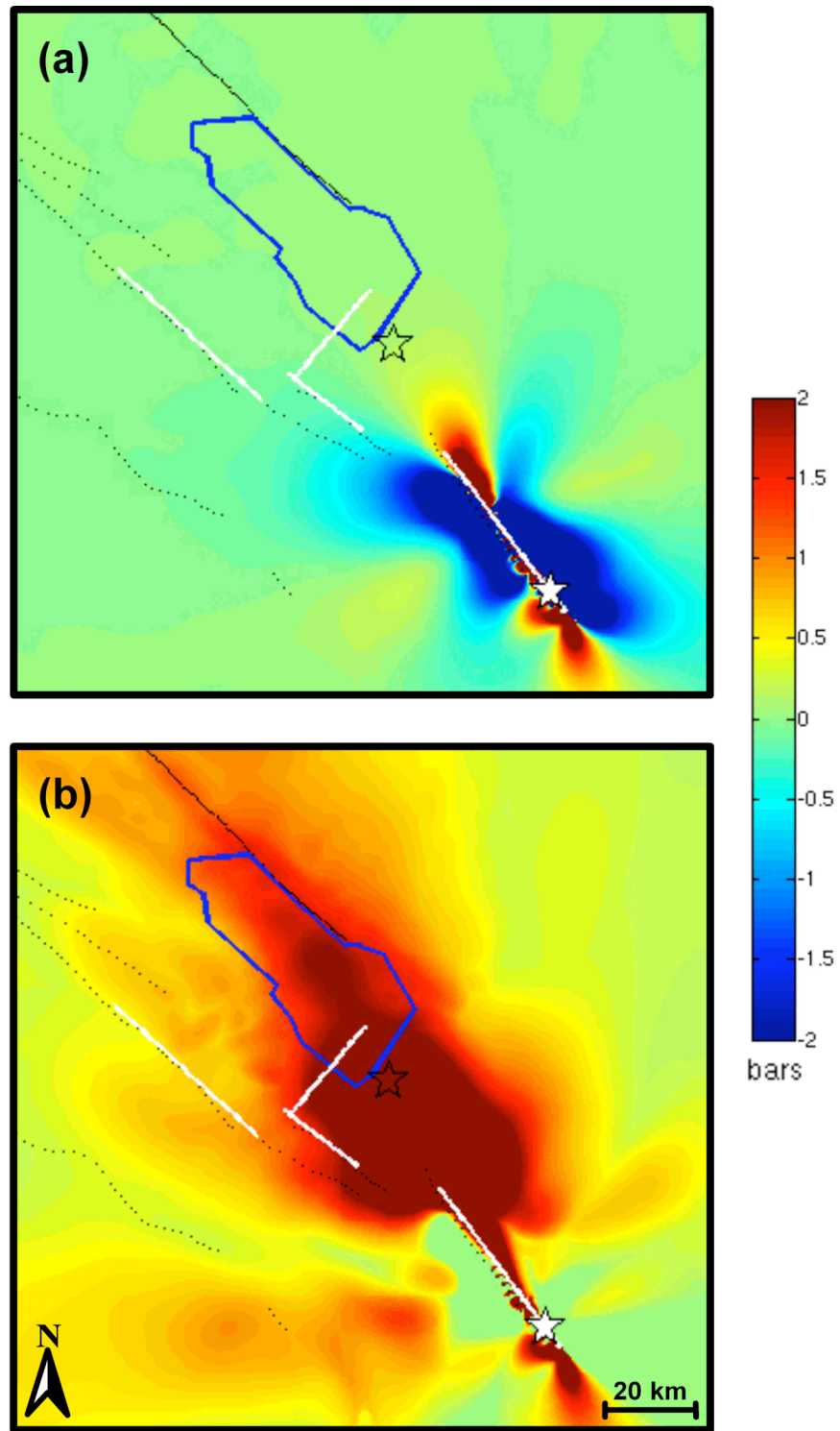


Figure 6

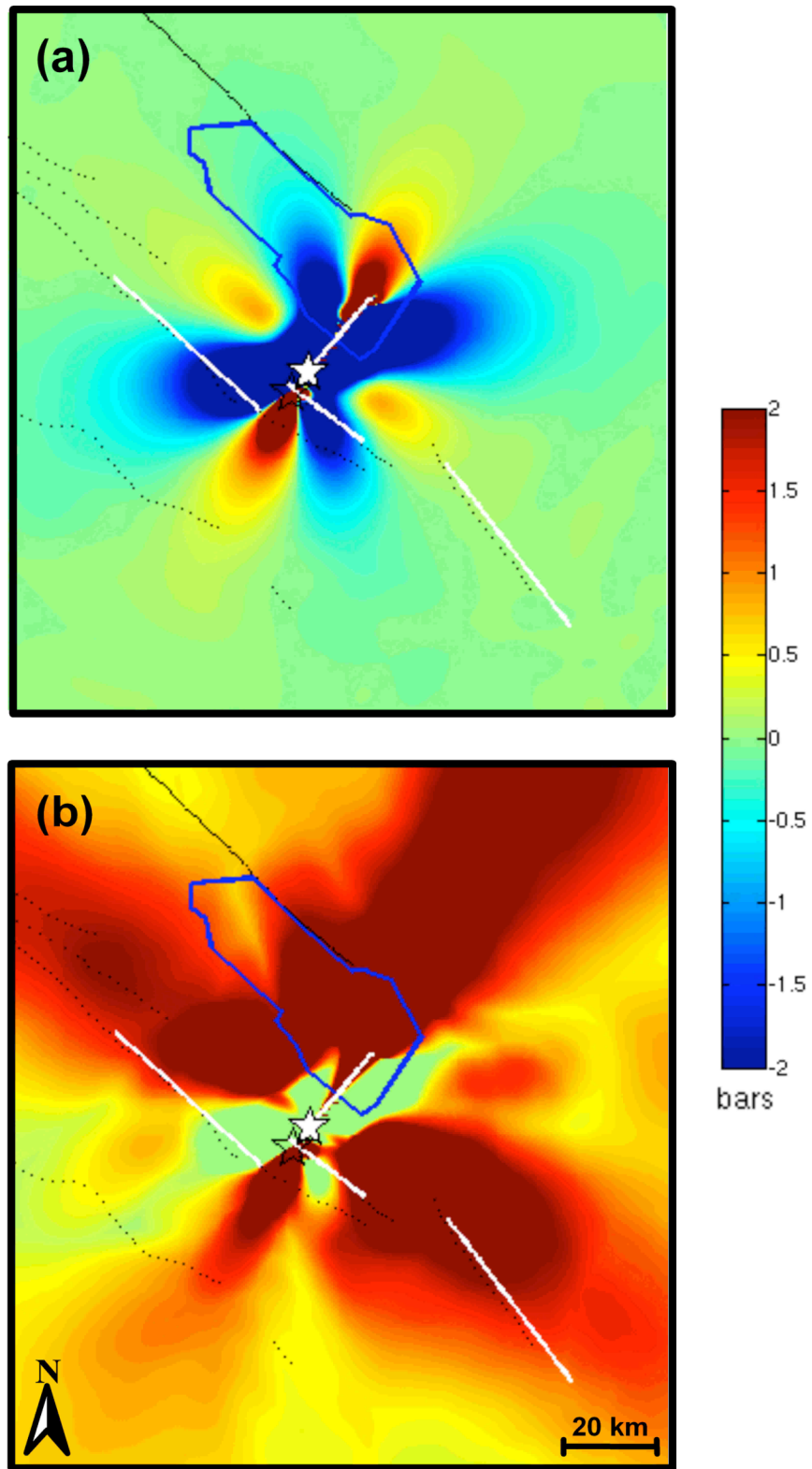


Figure 7

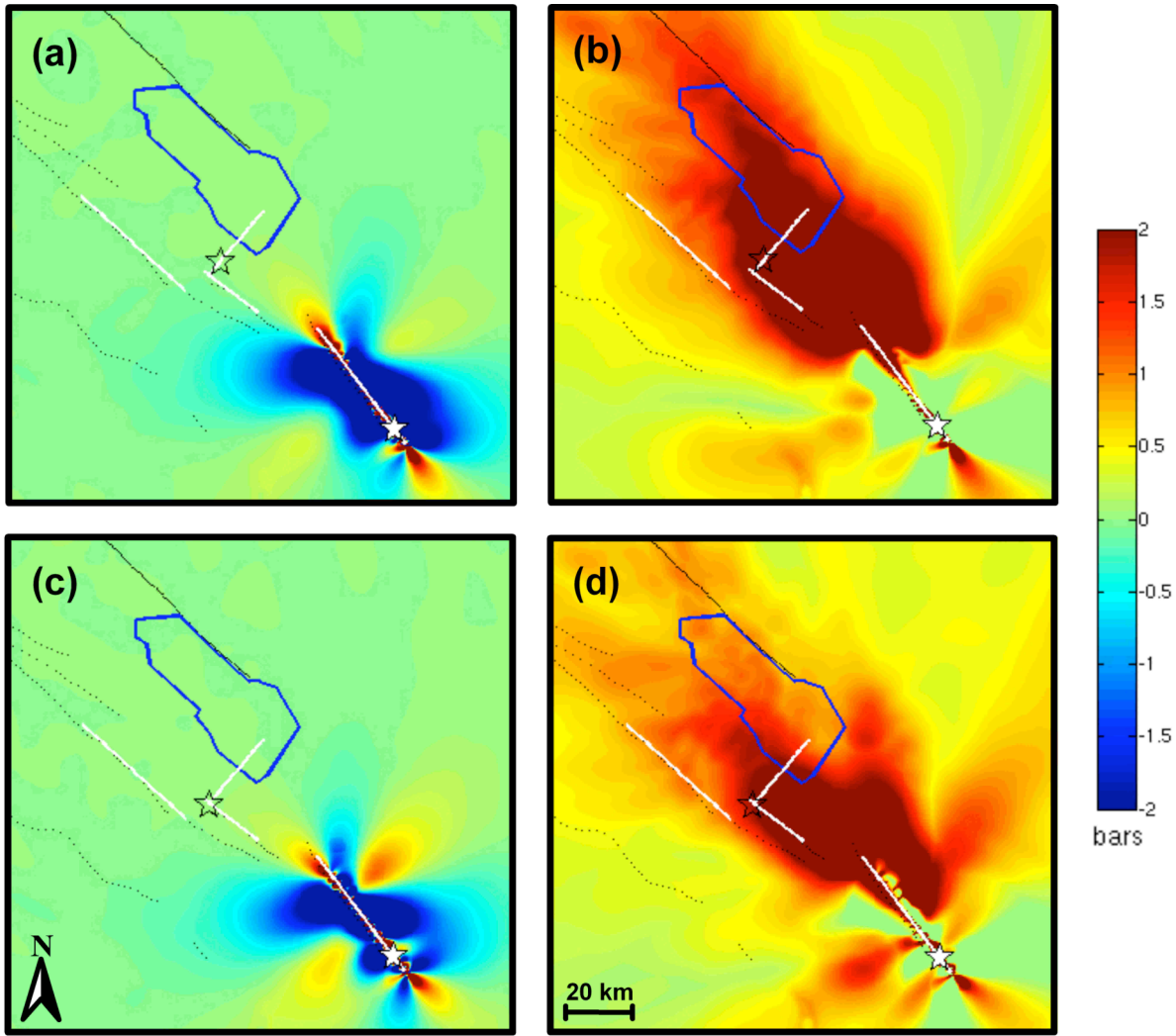


Figure 8

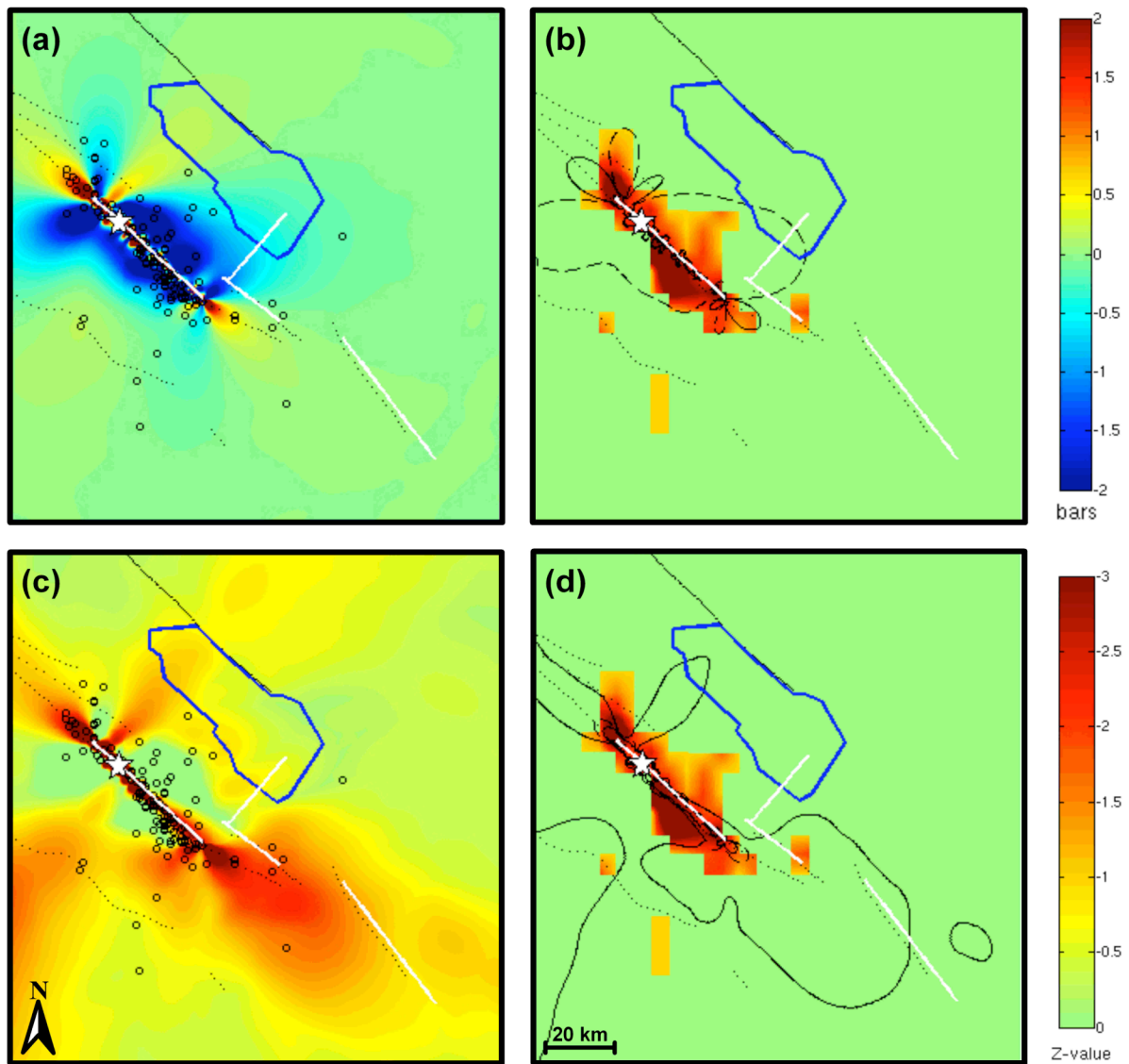


Figure 9

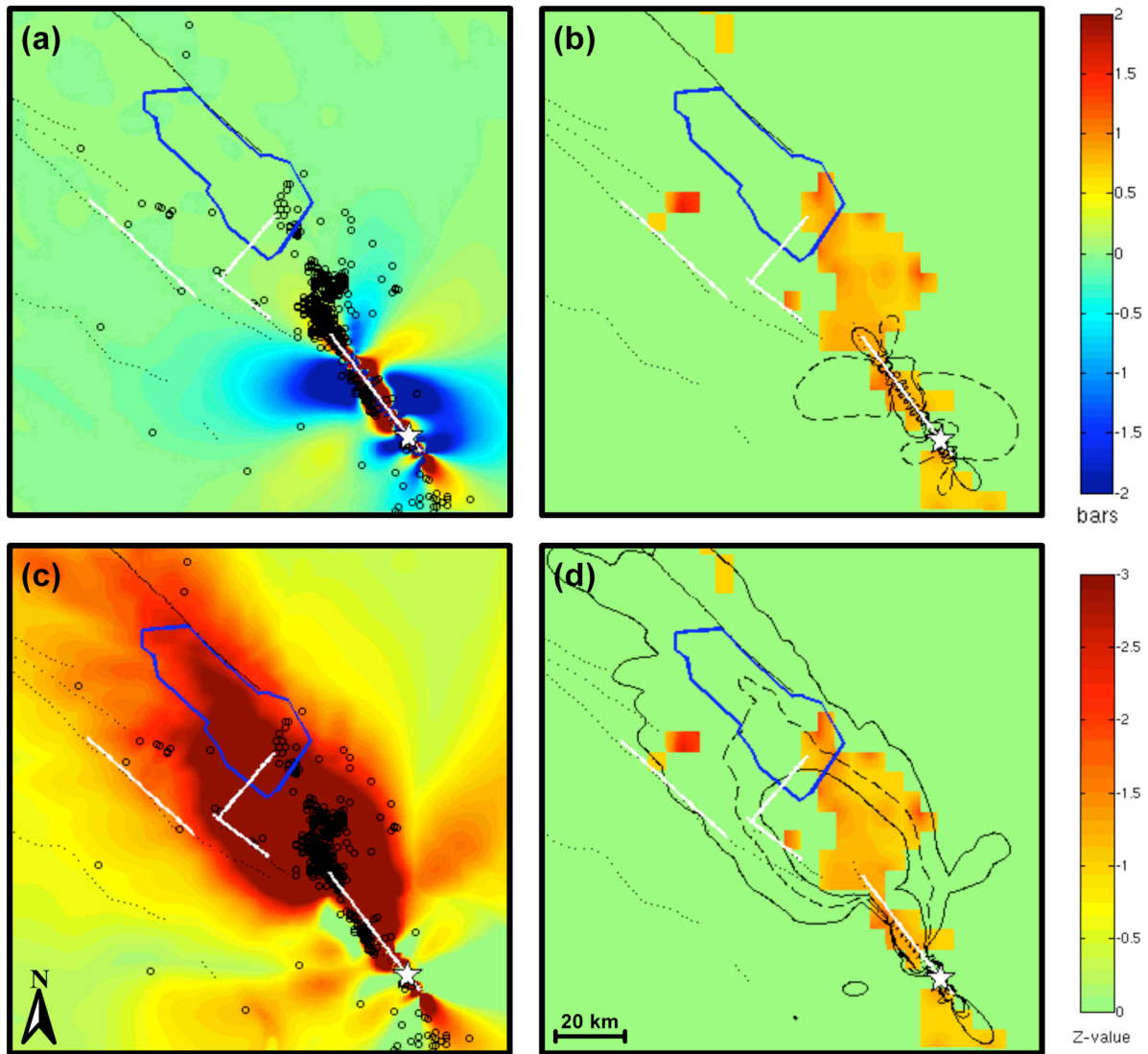


Figure 10

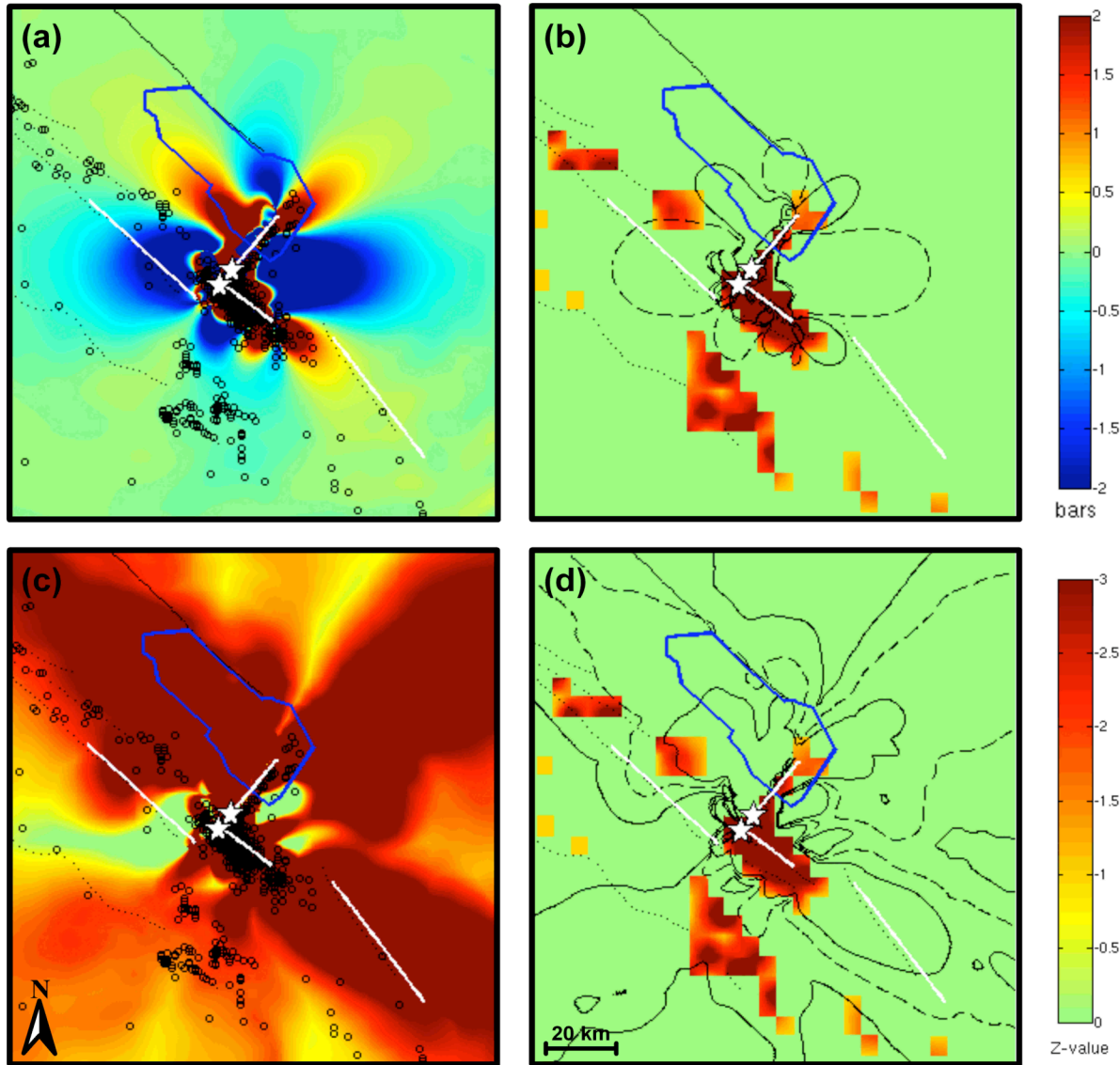


Figure 11

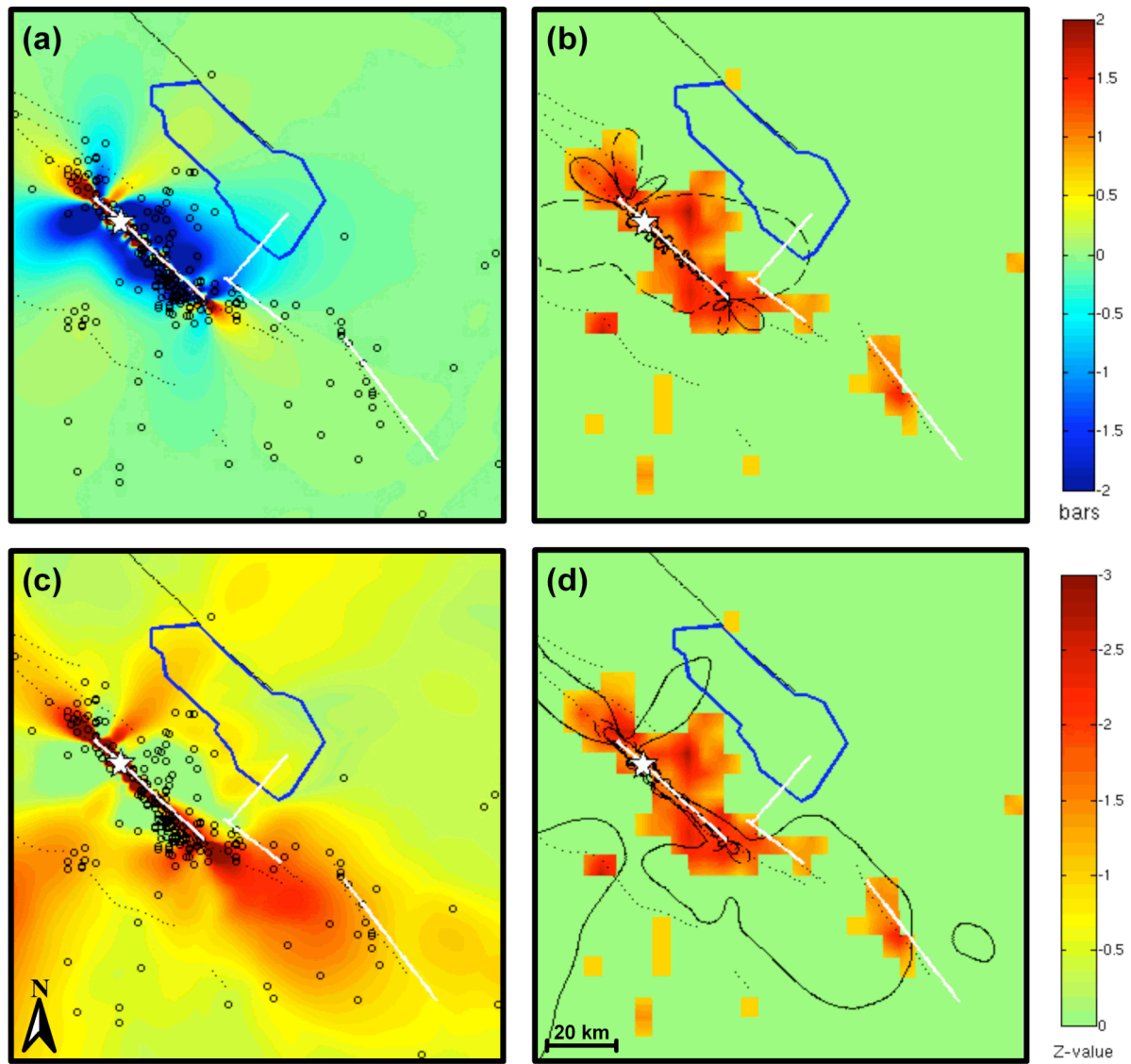


Figure 12

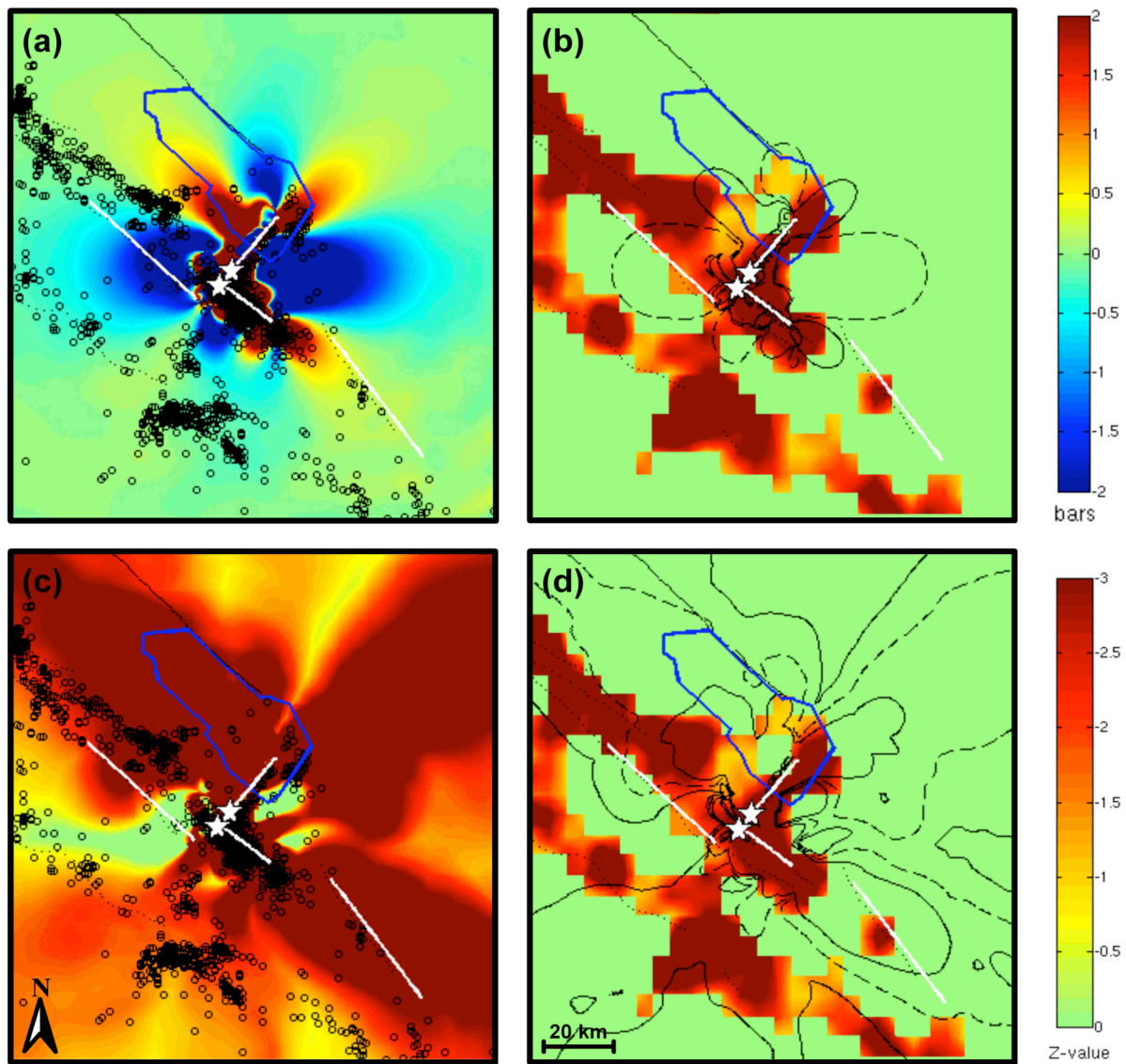


Figure 13

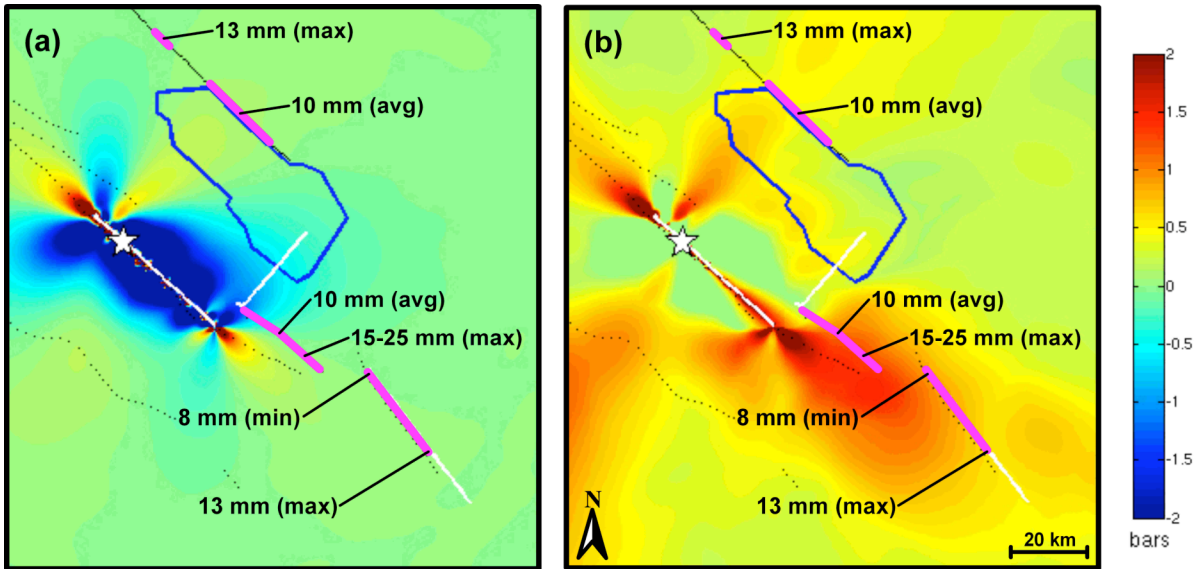


Figure 14

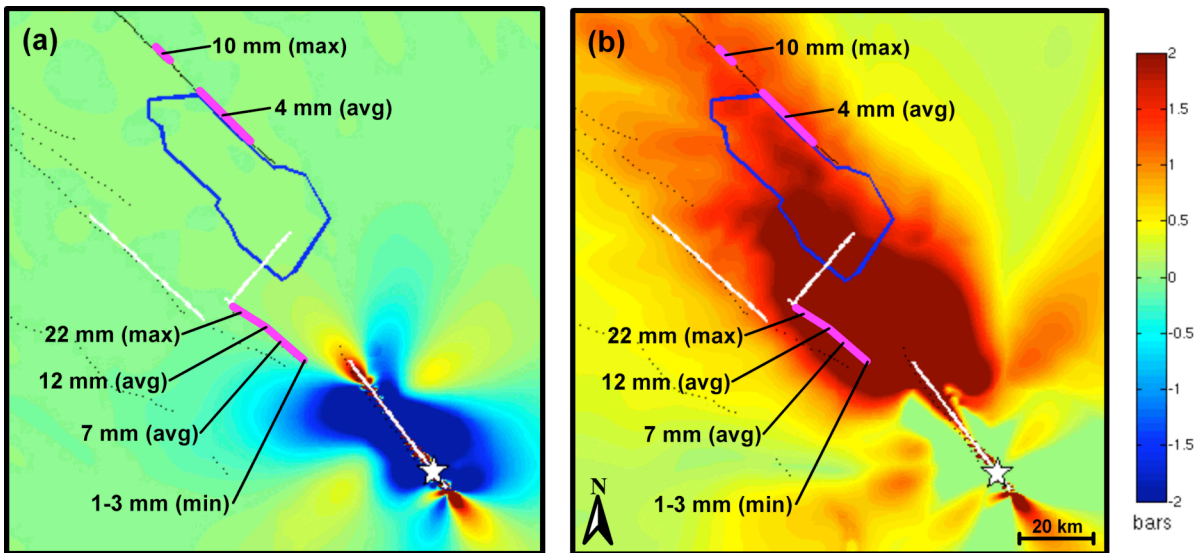


Figure 15

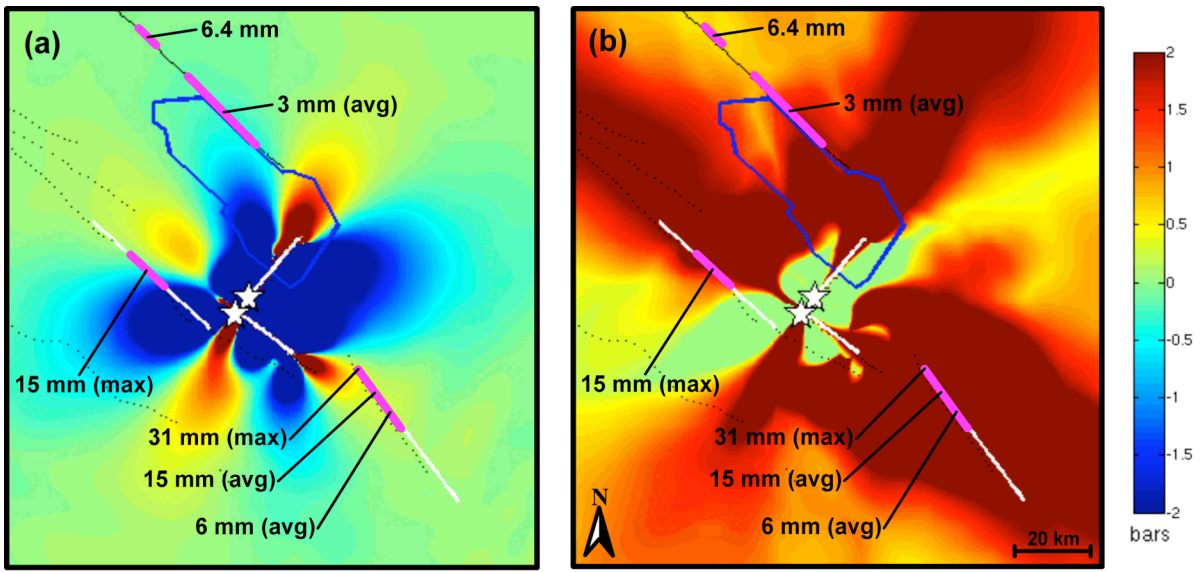


Figure 16

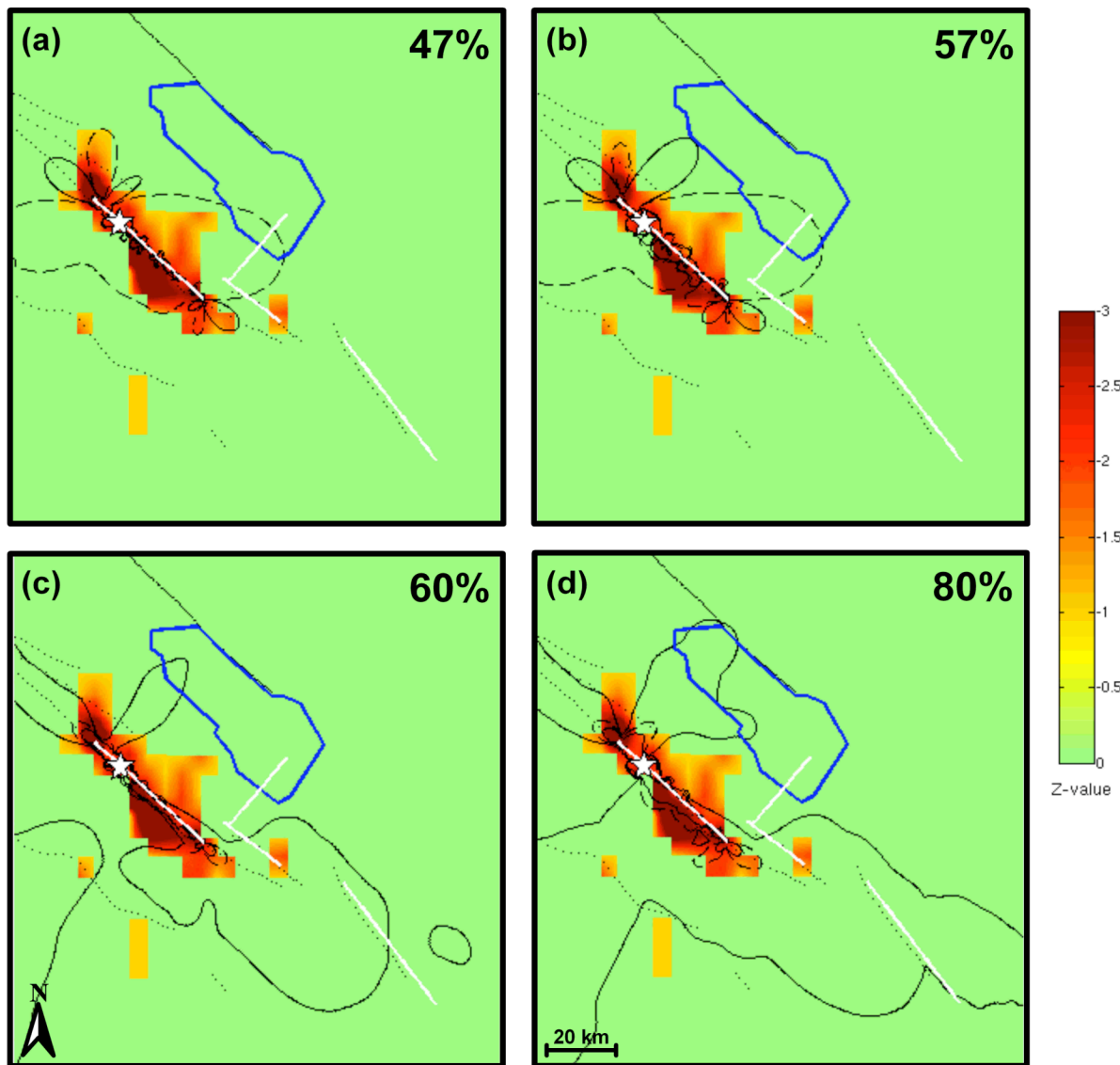


Figure A1

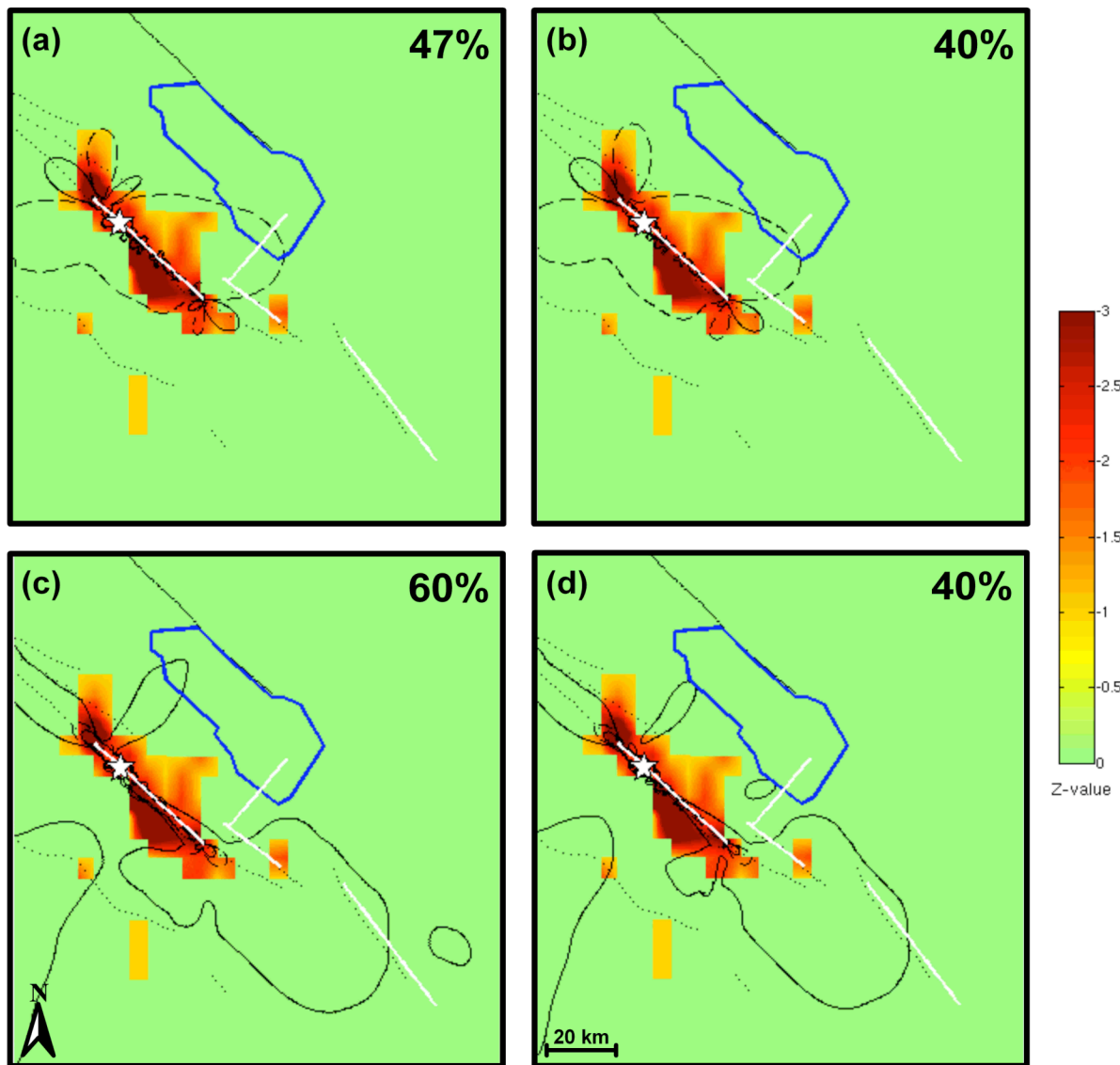


Figure A2

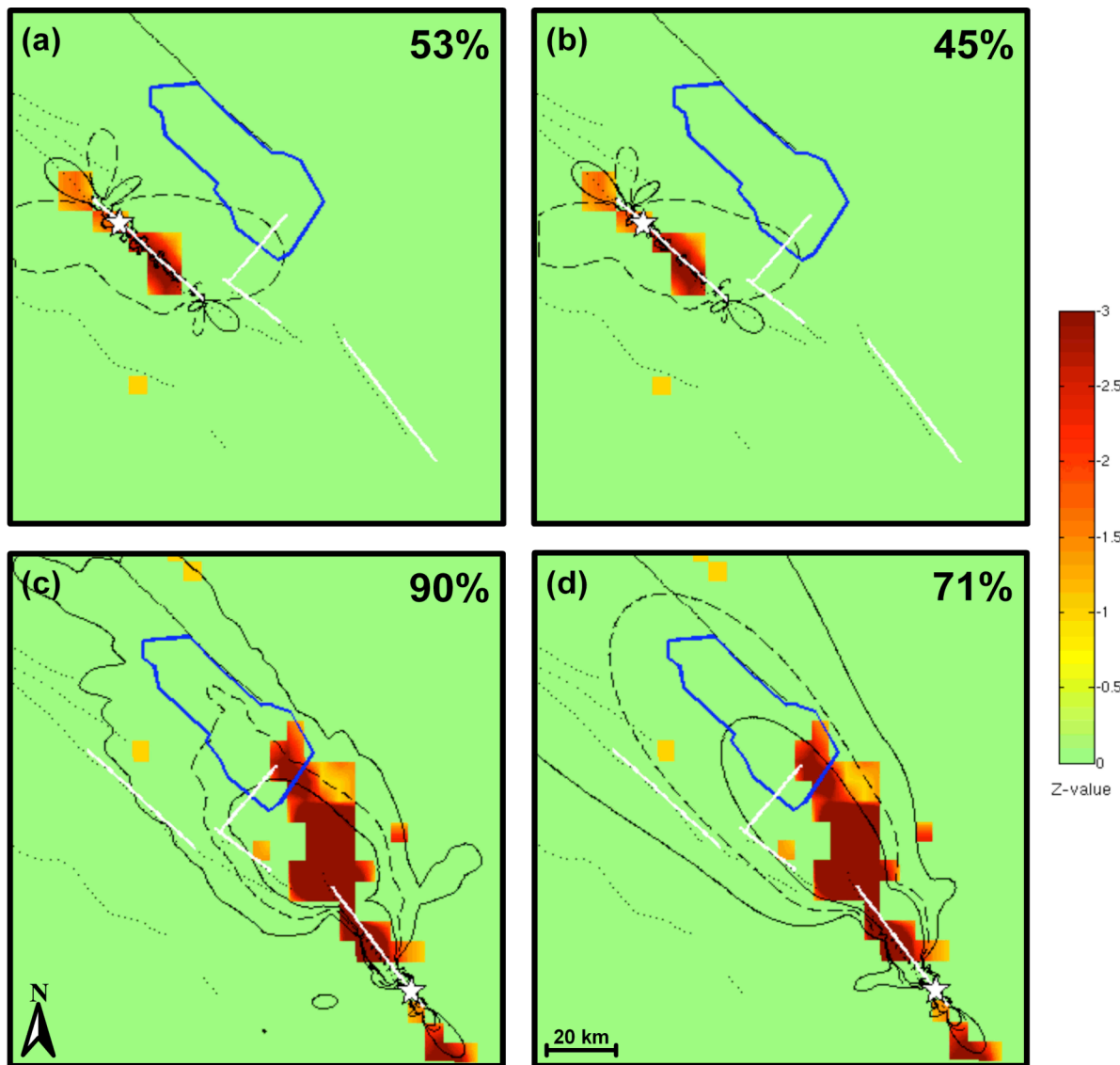


Figure A3

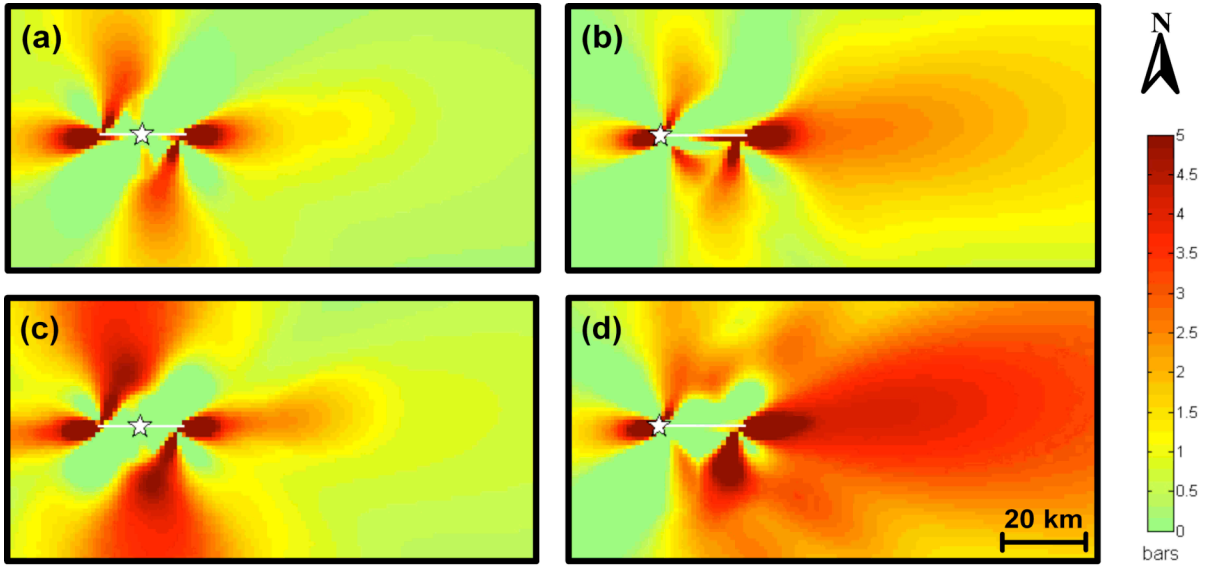


Figure A4